An Efficient Real-Time Planning Method for Swarm Robotics Based on an Optimal Virtual Tube

Pengda Mao, Shuli Lv, Chen Min, Zhaolong Shen, and Quan Quan, *Senior Member, IEEE*

arXiv:2505.01380v1 [cs.RO] 2 May 2025

Abstract—Swarm robotics navigating through unknown obstacle environments is an emerging research area that faces challenges. Performing tasks in such environments requires swarms to achieve autonomous localization, perception, decision-making, control, and planning. The limited computational resources of onboard platforms present significant challenges for planning and control. Reactive planners offer low computational demands and high re-planning frequencies but lack predictive capabilities, often resulting in local minima. Long-horizon planners, on the other hand, can perform multi-step predictions to reduce deadlocks but cost much computation, leading to lower re-planning frequencies. This paper proposes a real-time optimal virtual tube planning method for swarm robotics in unknown environments, which generates approximate solutions for optimal trajectories through affine functions. As a result, the computational complexity of approximate solutions is $O(n_t)$, where n_t is the number of parameters in the trajectory, thereby significantly reducing the overall computational burden. By integrating reactive methods, the proposed method enables low-computation, safe swarm motion in unknown environments. The effectiveness of the proposed method is validated through several simulations and experiments.

Index Terms—Trajectory planning, swarm robotics, multi-parameteric programming, optimal virtual tube

I. INTRODUCTION

Passing through an obstacle-dense environment safely and effectively is a focusing problem for swarm robotics, which could be applied in various fields, including search and rescue operations and environmental monitoring.

Swarm robotics trajectory planning can be categorized into centralized and distributed methods. In centralized trajectory planning, the host robot receives the state information of all robots within the swarm, plans collision avoidance trajectories for all robots, and then distributes the trajectories for each robot to execute trajectory tracking control. The advantages of the centralized trajectory planning method include the simplicity of algorithm deployment, reduction in location errors, and low hardware costs for the swarm. However, as the number of robots in the swarm increases, significant challenges arise in terms of communication maintenance and computational complexity. In contrast, distributed trajectory planning involves each robot independently planning its own trajectory to achieve collision avoidance and sharing its trajectory with neighboring robots via communication. This method allows robots to respond quickly to sudden situations. Distributed trajectory planning can be further divided into reactive planners

Pengda Mao, Shuli Lv, Chen Min, Zhaolong Shen, and Quan Quan are with School of Automation Science and Electrical Engineering, Beihang University, Beijing, 100191, P.R. China {maopengda, lvshuli, min_chen, shenzhaolong, qq_buaa}@buaa.edu.cn

Fig. 1: Trajectory overlap of swarm robots navigating through an unknown obstacle environment using the proposed method.

and long-horizon planners based on the length of prediction horizon [1].

Reactive planners, such as the potential field method and control barrier function (CBF), plan the next motion based on the current states of robots in neighbors. The advantages of reactive planners include low computational complexity, high replanning frequency, and minimal impact from communication delays. However, due to the lack of prediction steps, the reactive planners are prone to getting trapped in local minima and may exhibit less smooth movements. Long-horizon planners, on the other hand, predict multiple steps. These multi-step actions can be in discrete forms, such as model predictive control (MPC), or represented by parameterized trajectories, such as Bézier curves. The advantages of long-horizon planners include smoother movements and reduced deadlock due to the prediction horizon. However, the drawbacks of the long-horizon planners are also evident, as trajectory planning involves substantial computation costs and is sensitive to communication delays.

Recently, an efficient multi-trajectory planning method called optimal virtual tube planning [2] and a homotopic path planning algorithm named Tube-RRT* [3] were proposed. These methods demonstrated the feasibility of implementing centralized multiple trajectory planning on computationally constrained embedded platforms; however, a general real-time planning method for unknown environments remains a critical gap in current research. Therefore, this paper introduces a novel planning method that integrates centralized trajectory planning with distributed control, combining the strengths of both methods to achieve reliable and efficient swarm robotics navigation, as illustrated in Fig. 1. The trajectory planning is achieved through the use of multi-parametric programming,

which facilitates affine functions to approximate optimal trajectories. Since affine functions enable fast computations, the proposed method supports rapid replanning, ensuring both the responsiveness and smooth movements required for real-time swarm motions. The main contributions of this paper are as follows:

- A novel real-time planning framework based on the optimal virtual tube is proposed that combines centralized trajectory planning with distributed control. Specifically, one robot in the swarm plans an optimal virtual tube and shares it with all robots in the swarm, achieving centralized planning for trajectories. The task of collision avoidance is delegated to distributed control, enabling rapid responses to unexpected situations.

- The optimal virtual tube planning method is theoretically generalized to a more general formulation. Based on the theory of multi-parametric programming, the proposed method not only considers spatial trajectory planning but also integrates temporal trajectory planning, optimizing the total time required for swarm passing through obstacle environments. The optimal trajectory can be approximated by the affine functions, resulting in a computational complexity of $O(n_t)$, where n_t is the number of optimization variables. Moreover, the computational cost of the proposed method is independent of the number of generated trajectories, making it more suitable for multiple trajectory planning.

- The numerical simulations validate the theoretical effectiveness of the proposed method and analyze the effect of different parameters on its performance. By comparing the computational complexity with traditional methods, the superiority of the proposed method in terms of computation time is demonstrated. Finally, the real-time performance and effectiveness of the method are verified through several experiments in unknown obstacle environments.

II. RELATED WORK

This section will introduce the state-of-the-art methods, including reactive planners and long-horizon planners, in the trajectory planning of swarm robotics, pointing out their respective advantages and disadvantages, and then discuss the current research on the virtual tube for swarm robotics.

A. Reactive Planner

Reactive planners determine the commands for the next moment based on the current state. These methods include artificial potential field (APF), control barrier function (CBF), and bio-inspired methods. The artificial potential field (APF) method [4] is a traditional and effective method. Inspired by the concepts of electric and magnetic fields in physics, it translates the attraction to the goal and repulsion from obstacles or other robots into a mathematical model to guide robots from initial positions to target positions. Its advantages include simplicity, stability, and ease of implementation. However, it also faces challenges such as local minima [5] and nonsmooth commands. Many subsequent studies have focused on optimizing the potential field function and avoiding local minima [6]–[8]. The CBF method [9] is an optimization-based method that avoids collisions by introducing state constraints. It is suitable for precise control and scenarios with complex constraints. Compared to APF, CBF generates smoother control commands but requires more computational resources. Notably, APF has been proved as a special case of CBF for obstacle avoidance [10]. For the robotic swarm, the CBF is utilized to simultaneously achieve control objectives, collision avoidance, and connectivity maintenance, while ensuring that the feasible solution set for the QP problem is not empty [11]. In [12], the barrier function is extended from smooth functions to general nonsmooth functions, and the CBF method is employed to achieve collision avoidance both among robots in the swarm and with obstacles. Bio-inspired methods imitate the cooperative movement observed in schools of fish or flocks of birds to achieve coordinated motion in swarm robotics. The core principles involve three rules: avoiding collisions with nearby agents, aligning velocity with neighbors, and moving toward the center of the group. Classic algorithms include flocking [13] and Vicsek [14] model. These algorithms are advantageous for achieving swarm cohesion and are computationally simple. However, they cannot guarantee safety and are sensitive to parameter settings. Furthermore, in order to enhance the efficiency of the bio-inspired method while incorporating additional constraints, the optimization algorithm has emerged as a recent research focal point. The optimization algorithm leverages the foundational principles of the Boids model to define the optimization function for each robot, facilitating the achievement of control objectives in a distributed manner [15]–[17].

B. Long-horizon Planner

The long-horizon planner plans multi-step predictions for the robot based on the current states of the swarm and the shared multi-step predictions of adjacent robots. Compared to the reactive planner, it ensures smoother motion and reduces the likelihood of deadlock. However, it has a lower replanning frequency, higher computational cost, and is affected by communication delays. The multi-step predictions of the long-horizon planner can be represented in either discrete [18] or continuous forms [19]. A typical method of discrete forms is multi-agent Model Predictive Control (MPC). Unlike single-agent MPC, multi-agent MPC not only incorporates discrete models and obstacle avoidance constraints but also uses the shared discrete trajectories of other robots as collision avoidance constraints. This method is suitable for trajectory planning in complex, high-order systems, but the strong nonlinearity and numerous variables involved result in higher computational costs. Many studies have sought to improve computational efficiency for real-time planning by linearizing non-convex constraints and adding relaxation variables [20], [21]. In contrast, the continuous form of long-horizon planners usually employs parameterized trajectories, such as B-spline curves, to represent continuous multi-step predictions. This method helps mitigate issues related to excessive variables and lack of global information. However, trajectory planning

methods also face complex non-convex collision avoidance constraints and are unsuitable for precise control of complex systems due to the lack of consideration for the system model. Thus, many studies focus on simplifying these constraints. Some have introduced safe flight corridors (SFC) [22], used in single-robot planning, into multi-robot planning to simplify the representation of collision avoidance constraints. Others have transformed constrained optimization problems into unconstrained ones using penalty functions to accelerate computation [23]. Additionally, some studies have addressed the effect of communication delays by setting different planning states [24].

C. Virtual Tube

The "virtual tube" concept serves as a crucial safety area, delineating both the motion boundaries and directions for swarms. Originally conceived in the aerial traffic [25] to ensure safe airspace for unmanned aerial vehicles, these virtual tubes establish safeguarded aerial space, preventing conflicts with ground or airborne traffic. Building upon this foundation, Quan et al. [26] extended this concept, originally applied to single-vehicle flight, to the domain of swarm robotics. This virtual tube, devoid of internal obstacles, functions as a safety area and simplifies the control, which only needs to avoid inter-robot collisions and ensure non-contact with the boundary of the virtual tube. Moreover, expanding the applications to guiding swarms through passages, apertures, and around surveillance targets without divergence [27], [28], the virtual tube is extended to encompass the concept of "curved virtual tube" [29]. This curved virtual tube resembles road lanes for autonomous vehicles [30], [31], and corridors within multi-UAV frameworks [32].

In summary, the problem of the virtual tube can be divided into two core challenges—the *virtual tube planning problem* and the *virtual-tube-based passing-through control problem*. It should be noted that the methods mentioned above primarily address the passing-through control problem. For the virtual tube planning problem, the recent works [33], [34] outline a trajectory planning method yielding a generator curve through discrete waypoints via search-based methods. Subsequently, the virtual tube emerges via the expansion of this generator curve, meticulously avoiding obstacles. To plan the virtual tube in the high-dimension space, a virtual tube without a generator curve is defined, and an optimal virtual tube is proposed to generate infinite optimal trajectories [2], [3]. However, an efficient planning framework is needed to achieve real-time planning of the optimal virtual tube in unknown obstacle environments. Furthermore, previous works focused on specific piecewise polynomial trajectories and assumed consistent time allocations. Thus, there is a need to generalize the planning method to accommodate different trajectory representations and objectives.

III. PRELIMINARIES AND PROBLEM FORMULATION

This section introduces the background of the virtual tube planning problem. The trajectory is parameterized using Bézier curves, while the virtual tube is defined as a set of four tuples within the free space to guide the flow of swarm robotics. The robot is modeled as a mass point, and finally, the problem formulation is presented in detail.

A. Trajectory Parameterization

It is common to employ a Bézier curve of degree p to represent the trajectory, leveraging the convex hull property that confines the curve within the control polygons. Let the set of control points be $\mathbf{P} = \begin{bmatrix} \mathbf{p}_0 & \mathbf{p}_1 & \cdots & \mathbf{p}_p \end{bmatrix} \in {}^{3 \times (p+1)}$ and the domain be $t \in [0, \Delta t]$. The Bézier curve is represented by

$$\mathbf{h}(t) = \sum_{k=0}^{p} B_{p,k}(t)\mathbf{p}_k \tag{1}$$

where $\mathbf{h}(0) = \mathbf{p}_0$, $\mathbf{h}(\Delta t) = \mathbf{p}_p$ and the basis functions $B_{p,k}(t)$ are expressed as

$$B_{p,k}(t) = \frac{p!}{k!(p-k)!} \left(\frac{t}{\Delta t} \right)^k \left(1 - \frac{t}{\Delta t} \right)^{p-k}.$$

And the derivative of the Bézier curve in (1) is expressed as

$$\dot{\mathbf{h}}(t) = \sum_{k=0}^{p-1} B_{p-1,k}(t)\mathbf{q}_k \tag{2}$$

where $\mathbf{q}_k$ are defined as follows:

$$\mathbf{q}_k = \frac{p}{\Delta t}(\mathbf{p}_{k+1} - \mathbf{p}_k). \tag{3}$$

Similarly, the derivative of the Bézier curve is bounded by the control points $\mathbf{q}_k$, which is useful for constraining high-order systems.

The representation of the Bézier curve in matrix form is useful for the optimization problem. While there is a non-standard representation, specific degrees of Bézier curves have been derived, as detailed in [35]. For example, a cubic Bézier curve can be written as

$$\mathbf{h}(t) = \boldsymbol{\beta}(t)\mathbf{S}_{\Delta t}\mathbf{M}\mathbf{P}^{\mathrm{T}} \tag{4}$$

where $\boldsymbol{\beta}(t) = [1 \ t \ t^2 \ t^3]$,

$$\mathbf{S}_{\Delta t} = \begin{bmatrix} 1 & 0 & 0 & 0 \\ 0 & \frac{1}{\Delta t} & 0 & 0 \\ 0 & 0 & \frac{1}{\Delta t^2} & 0 \\ 0 & 0 & 0 & \frac{1}{\Delta t^3} \end{bmatrix},$$

$$\mathbf{M} = \begin{bmatrix} 1 & 0 & 0 & 0 \\ -3 & 3 & 0 & 0 \\ 3 & -6 & 3 & 0 \\ -1 & 3 & -3 & 1 \end{bmatrix}.$$

B. Virtual Tube

Intuitively, a virtual tube is defined by maps between two bounded convex sets in free space. The virtual tube is defined as the following:

Definition 1. *A virtual tube $\mathcal{T}$ [2], as shown in Fig. 2, is a set in n-dimension space represented by a 4-tuple $(\mathcal{C}_0, \mathcal{C}_1, \mathbf{f}, \mathbf{h})$ where*
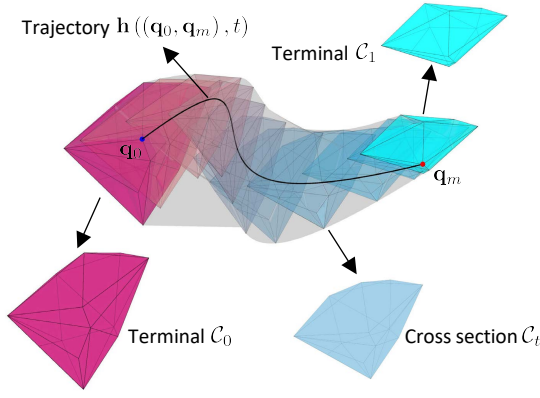
Fig. 2: An example of a virtual tube. The purple and blue polyhedrons are terminals. The shaded polyhedrons are cross sections $\mathcal{C}_t$. The black curve is a trajectory that is from $\mathbf{q}_0$ in terminal $\mathcal{C}_0$ to $\mathbf{q}_m$ in terminal $\mathcal{C}_1$. The gray area is the virtual tube. [2]

- $\mathcal{C}_0, \mathcal{C}_1$, *called* terminals, *are disjoint bounded convex subsets in n-dimension space.*
- $\mathbf{f}$ *is a* diffeomorphism: $\mathcal{C}_0 \rightarrow \mathcal{C}_1$, *so that there is a set of order pairs* $\mathcal{P} = \{(\mathbf{q}_0, \mathbf{q}_m) \,|\, \mathbf{q}_0 \in \mathcal{C}_0, \mathbf{q}_m = \mathbf{f}(\mathbf{q}_0) \in \mathcal{C}_1\}$.
- $\mathbf{h}$ *is a smooth[1] map:* $\mathcal{P} \times \mathcal{I} \rightarrow \mathcal{T}$ *where* $\mathcal{I} = [0,1]$, *such that* $\mathcal{T} = \{\mathbf{h}((\mathbf{q}_0, \mathbf{q}_m), t) \,|\, (\mathbf{q}_0, \mathbf{q}_m) \in \mathcal{P}, t \in \mathcal{I}\}$, $\mathbf{h}((\mathbf{q}_0, \mathbf{q}_m), 0) = \mathbf{q}_0$, $\mathbf{h}((\mathbf{q}_0, \mathbf{q}_m), 1) = \mathbf{q}_m$. *The function* $\mathbf{h}((\mathbf{q}_0, \mathbf{q}_m), t)$ *is called a* trajectory *for a order pair* $(\mathbf{q}_0, \mathbf{q}_m)$.

And, a cross-section $\mathcal{C}$ of a virtual tube at $t \in \mathcal{I}$ is expressed as:

$$\mathcal{C}_t = \{\mathbf{h}((\mathbf{q}_0, \mathbf{q}_m), t) \,|\, (\mathbf{q}_0, \mathbf{q}_m) \in \mathcal{P}\}. \tag{5}$$

The surface of the virtual tube is the boundary of $\mathcal{T}$, defined as $\partial \mathcal{T}$.

And if each trajectory in the virtual tube is optimal, then the virtual tube is optimal. The definition of optimal virtual tube is as follows.

Definition 2. *A virtual tube $\mathcal{T}^*$ is* optimal *with respect to a cost g if every trajectory $\mathbf{h}^*$ in the tube is* optimal *with respect to a cost g, namely $\mathcal{T}^* = (\mathcal{C}_0, \mathcal{C}_1, \mathbf{f}, \mathbf{h}^*)$.*

C. Robot Model

The robot in swarm is regarded as a mass point which is expressed as

$$\dot{\mathbf{p}}_i = \mathbf{v}_{c,i} \tag{6}$$

where $\mathbf{p}_i$ is the position of the i-th robot and $\mathbf{v}_{c,i}$ is the velocity command for the i-th robot in swarm. According to [26], there are three areas around the robot: safety, avoidance, and other areas. The safety area is a sphere with a radius r_s centered into the center of mass of the robot to represent the physical shape of the robot. If other robots enter the

[1]A real-valued function is said to be smooth if its derivatives of all orders exist and are continuous.
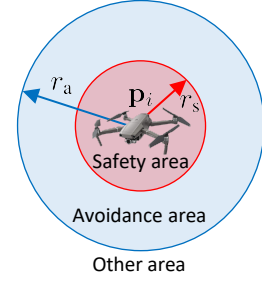

Fig. 3: The robot model. The red and blue areas represent the safety area with a radius r_s and the avoidance area with a radius r_a, respectively.

safety area, a collision may happen. Thus, other robots are not allowed to enter the safety area. And the avoidance area is a sphere with a radius r_a centered in the center of mass of the robot to avoid other robots. When the avoidance area has intersection with safety areas of other robots, avoidance motions are triggered. When other robots are in the other area, there is no avoidance between them.

D. Multi-Parametric Programming

Multi-parametric programming is a paradigm that considers the change of solution of a constrained optimization problem as a function of parameters. Multi-parametric programming detaches from the sensitivity analysis theory. Compared with the research, the process conditions deviate from the nominal values to its neighborhood; multi-parametric programming is concerned with the whole range of the parameters. The multi-parametric linear programming (mp-LP) problem is one of the main classes of parametric programming problems [36]. A multi-parametric linear programming problem is defined as

$$V(\boldsymbol{\theta}) = \min_{\mathbf{x} \in \mathbb{R}^n} \quad \mathbf{c}^{\mathrm{T}}\mathbf{x}$$
$$\text{s.t.} \quad \mathbf{A}\mathbf{x} \leq \mathbf{b} + \boldsymbol{F}\boldsymbol{\theta} \tag{7}$$
$$\boldsymbol{\theta} \in \boldsymbol{\Theta},$$

where $\mathbf{c} \in \mathbb{R}^n$, $\mathbf{A} = \begin{bmatrix} \mathbf{a}_1^{\mathrm{T}} & \cdots & \mathbf{a}_{k_p}^{\mathrm{T}} \end{bmatrix}^{\mathrm{T}} \in \mathbb{R}^{k_p \times k_q}$, $\mathbf{b} = \begin{bmatrix} b_1 & \cdots & b_{k_p} \end{bmatrix}^{\mathrm{T}} \in \mathbb{R}^{k_p}$, and $\mathbf{F} = \begin{bmatrix} \mathbf{f}_1^{\mathrm{T}} & \cdots & \mathbf{f}_{k_p}^{\mathrm{T}} \end{bmatrix}^{\mathrm{T}} \in \mathbb{R}^{k_p \times k_q}$ are constants in constraints, k_p is the rows of constraints and k_q is the dimension of the parameter $\boldsymbol{\theta}$. The solution to (7) is given by the partitioning of the feasible parameter space $\boldsymbol{\Theta}_f \subset \boldsymbol{\Theta}$ into polytopic regions, namely *critical regions* (CR). Each region is associated with a optimal solution $\mathbf{x}(\boldsymbol{\theta})$ and a value of the objective function $V(\boldsymbol{\theta})$, both of which are affine functions of $\boldsymbol{\theta}$ [37].

The first-order Karush-Kuhn-Tucker (KKT) optimality conditions for (7) are given as

$$\mathcal{L} = \mathbf{c}^{\mathrm{T}}\mathbf{x} + \boldsymbol{\lambda}^{\mathrm{T}}(\mathbf{A}\mathbf{x} - \mathbf{b} - \mathbf{F}\boldsymbol{\theta}),$$
$$\nabla \mathcal{L} = \mathbf{c} + \mathbf{A}^{\mathrm{T}}\boldsymbol{\lambda} = \mathbf{0}, \tag{8}$$
$$(\mathbf{A}\mathbf{x} - \mathbf{b} - \mathbf{F}\boldsymbol{\theta})\,\mathrm{diag}(\boldsymbol{\lambda}) = \mathbf{0}, \boldsymbol{\lambda} \geq \mathbf{0}.$$
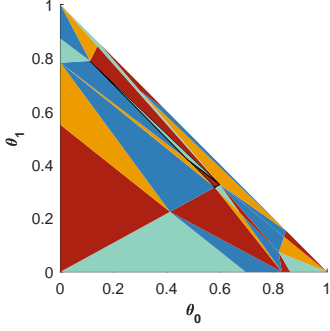
Fig. 4: An example of critical regions with the parameter $\boldsymbol{\theta} = [\theta_0 \; \theta_1]$. Different colors represent different critical regions.

According to the basic sensitivity theorem [38], in the neighborhood of the KKT point $[\mathbf{x}(\boldsymbol{\theta}_0), \boldsymbol{\lambda}(\boldsymbol{\theta}_0)]^{\mathrm{T}}$, the optimal solution could be expressed as a continuous piecewise affine:

$$\begin{bmatrix} \mathbf{x}(\boldsymbol{\theta}) \\ \boldsymbol{\lambda}(\boldsymbol{\theta}) \end{bmatrix} = -\mathbf{M}^{-1}\mathbf{N}(\boldsymbol{\theta} - \boldsymbol{\theta}_0) + \begin{bmatrix} \mathbf{x}(\boldsymbol{\theta}_0) \\ \boldsymbol{\lambda}(\boldsymbol{\theta}_0) \end{bmatrix}, \quad (9)$$

where

$$\mathbf{M} = \begin{bmatrix} \mathbf{0} & \mathbf{a}_1^{\mathrm{T}} & \cdots & \mathbf{a}_{k_p}^{\mathrm{T}} \\ -\lambda_1\mathbf{a}_1 & -\mathbf{v}_1 & & \\ \vdots & & \ddots & \\ -\lambda_{k_p}\mathbf{a}_{k_p} & & & -\mathbf{v}_{k_p} \end{bmatrix},$$

$\mathbf{N} = \begin{bmatrix} \mathbf{0} \; \lambda_1\mathbf{f}_1 \; \cdots \; \lambda_{k_p}\mathbf{f}_{k_p} \end{bmatrix}^{\mathrm{T}}$, $\mathbf{v}_k = \mathbf{a}_k\mathbf{x}(\boldsymbol{\theta}_0) - b_k - \mathbf{f}_k\boldsymbol{\theta}_0$, $k = 1, 2, ..., k_p$. Each set of parametric solutions is obtained, and then the corresponding CR is obtained, as shown in Fig. 4.

As only the uncertainty of right-hand side is present in problem (7) which is not suitable for more general applications, many studies considered the question of left-hand side multiparametric programming problems, i.e.,

$$\begin{aligned} \mathbf{A}(\boldsymbol{\theta})\mathbf{x} &\le \mathbf{b} + \mathbf{F}\boldsymbol{\theta}, \\ \mathbf{A}(\boldsymbol{\theta}) &= \mathbf{A}_1 + \sum_{k=1}^{k_q} \theta_k \mathbf{A}_{k+1}. \end{aligned} \quad (10)$$

Having obtained critical regions, once the parameter $\boldsymbol{\theta}$ is set, the corresponding critical region is set, and the optimal solution $\mathbf{x}(\boldsymbol{\theta})$ is obtained directly, which could efficiently reduce the computational complexity in real-time planning problem.

E. Problem Formulation

Suppose there is a swarm of robots with the number $N+1$ in an unknown obstacle environment, which is represented as a set $\mathcal{N} = \{i\} \, (i = 0, 1, ..., N)$. Let the start area and goal area be $\mathcal{C}_0$ and $\mathcal{C}_1$ in free space. The main problem is to plan an optimal virtual tube $\mathcal{T}^* = (\mathcal{C}_0, \mathcal{C}_1, \mathbf{f}, \mathbf{h}^*)$ in free space of the obstacle-dense environment so that each robot $i \in \mathcal{N}$ is assigned an optimal trajectory $\mathbf{h}_i^*(t), t \in [0, T_i]$ in $\mathcal{T}^*$ which satisfies the following conditions:

- The trajectory $\mathbf{h}_i^*(t)$ is feasible for the dynamics of robot i.

- The trajectory $\mathbf{h}_i^*(t)$ is from the start position $\mathbf{s}_i \in \mathcal{C}_0$ to the goal position $\mathbf{g}_i \in \mathcal{C}_1$ such that $\mathbf{h}_i^*(0) = \mathbf{s}_i$, $\mathbf{h}_t^*(T_i) = \mathbf{g}_i$, where T_i is the total time for the robot i.
- The robot i needs to minimize the total time T_i required to move from the start position $\mathbf{s}_i$ to the goal position $\mathbf{g}_i$.
- The robot i is stationary at the start and goal position such that $\frac{\mathrm{d}^k\mathbf{h}_t^*(0)}{\mathrm{d}t^k} = \frac{\mathrm{d}^k\mathbf{h}_t^*(T_i)}{\mathrm{d}t^k} = 0, k \ge 1$.

Meanwhile, a suitable controller is selected to make robot i track its own trajectory and avoid other robots j in the virtual tube, which is expressed as $\|\mathbf{p}_i(t) - \mathbf{p}_j(t)\| \ge 2r_s, t \in [0, \min(T_i, T_j)], \forall j \in \mathcal{N}\backslash i$.

IV. ARCHITECTURE OVERVIEW

A. Framework

The framework of the proposed planning method, as shown in Fig. 5, includes a planner and controller. Only the host robot named Robot 0 in the swarm has both planner block and controller block, and others named Robot $1 \sim N$ have only controller blocks. The functions of all blocks are described in the following.

Planner: The module of homotopic path planning receives the information from on-board sensors to generate the boundary homotopic paths $\{\boldsymbol{\sigma}_k\}$ $(k = 1, 2, ..., k_c)$ of the virtual tube. Then, the module of optimal virtual tube planning uses the boundary paths $\{\boldsymbol{\sigma}_k\}$ as the input and generates the optimal virtual tube $\mathcal{T}^*$.

Controller: The robot receives the optimal virtual tube $\mathcal{T}^*$ via broadcast communication for other robots or internal interface for Robot 0. Then, the optimal trajectory $\mathbf{h}_i^*$ for robot i is generated from optimal virtual tube $\mathcal{T}^*$ by affine functions. Subsequently, the controller combines trajectory tracking and collision avoidance to ensure that the robot can arrive at the goal position while avoiding other robots and tube boundaries.

The framework employs two communication methods: **centralized optimal virtual tube planning** and **distributed control**. In centralized optimal virtual tube planning, the optimal virtual tube is planned on Robot 0 and then distributed to all robots in the swarm via the communication network denoted as ① in Fig. 5. In distributed control, each robot obtains the pose information of nearby robots and shares its own pose information denoted as ② in Fig. 5 to achieve trajectory tracking and collision avoidance.

B. Replanning Strategy

In the proposed method, since the optimal virtual tube is shared by all robots in the swarm, only a single shared virtual tube needs to be planned. As shown in Fig. 6, all obstacles within the detection range are known, while it is assumed there are no obstacles outside the detection range. The planner uses the current obstacle information to plan a whole virtual tube to the goal area, as indicated by the red curves in Fig. 6. However, the whole tube is likely to collide with unknown obstacles outside the detection range. To ensure safety, the portion of the tube within the detection range is designated as the committed tube, meaning it will no longer be updated. When robots in the swarm move beyond the committed tube, the virtual
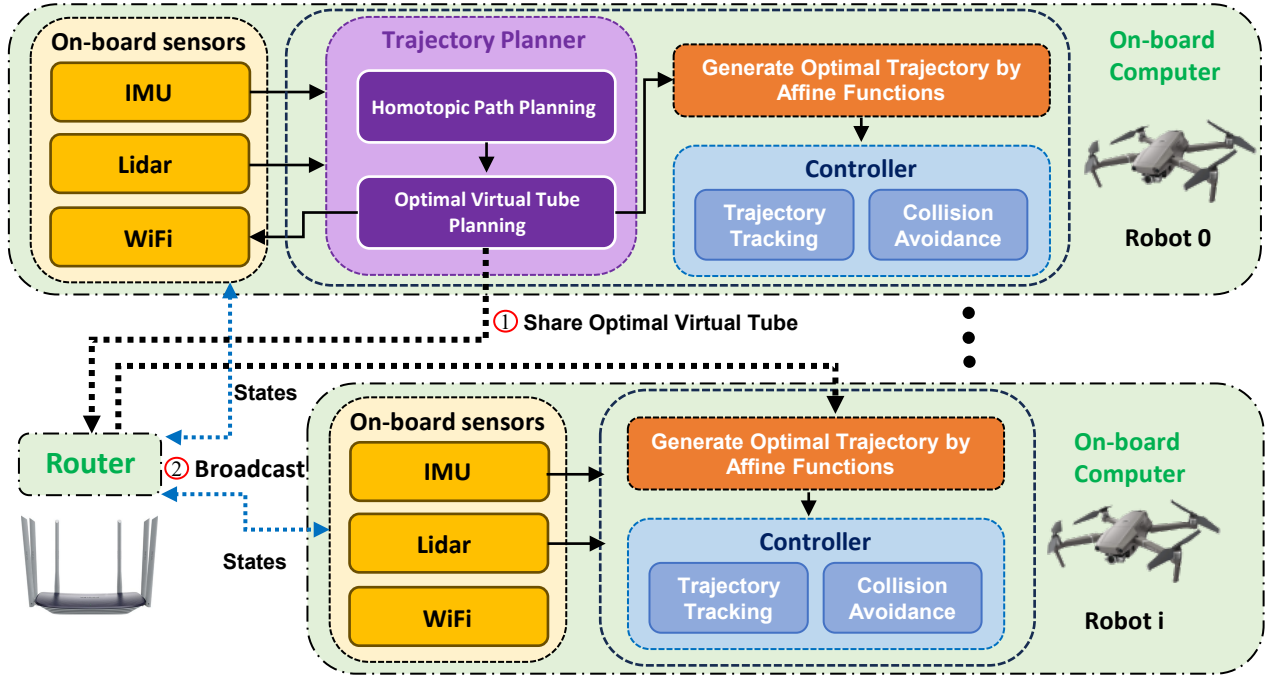
Fig. 5: The framework of the proposed planning method. All robots have the same controller, and only Robot 0 has the planner block. The optimal virtual tube is planned by Robot 0 and shared with other robots by ①. The states of robots are shared by the broadcast ②. Other robots receive states and the optimal virtual tube to generate the optimal trajectory by affine functions. Then, the controllers of robots achieve trajectory tracking and collision avoidance.
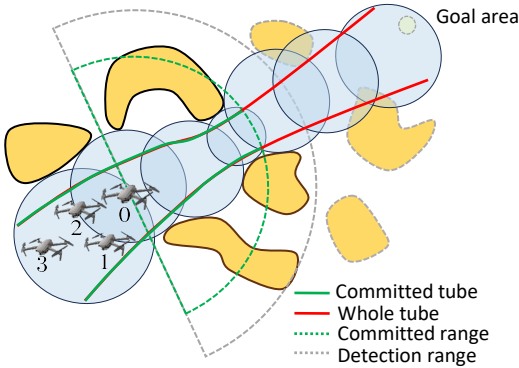

Fig. 6: The replanning strategy of the proposed method. The known and unknown obstacles are colored orange and light orange, respectively. The boundary of the committed virtual tube and the whole virtual tube are represented by green and red curves. The sensing range and committed range are denoted by gray and green semicircles, respectively.

tube is replanned. Compared to other swarm trajectory update strategies, this method aligns the update frequency with that of single-robot trajectory planning [39], [40]. Additionally, by delegating obstacle avoidance to the control level, the frequency of obstacle avoidance is significantly increased, enabling a faster response to obstacles.

V. METHODS

The process of optimal virtual tube planning could be divided into two steps: homotopic path planning and optimal virtual tube planning. The first step, homotopic path planning, uses a suitable path planning algorithm to generate the homotopic paths for the virtual tube. Then, the second step, optimal virtual tube planning, plans the optimal virtual tube based on these path points. We detail these two steps in the following.

A. Homotopic Path Planning

An infinite homotopic path planning method, named Tube-RRT* [3], has been proposed for virtual tube planning, which is inspired by the single-robot path planning methods in [39], [41]. Tube-RRT* is a sample-based path planning method that samples intersected spheres in free space denoted by blue circles in Fig. 6 and plans a sequence of spheres from the start area to the goal area. The boundary paths $\boldsymbol{\sigma}_k(k = 1, 2, ..., k_c)$ for the virtual tube are selected in the sequence of spheres to be used for the trajectory optimization in the following.

B. Optimal Virtual Tube Planning

In the previous work [2], the trajectory is parameterized by the piece-wise continue polynomials. There is a problem with this parameterization method, which is not theoretically able to guarantee that the trajectory remains within the safe region. Meanwhile, the desired total times for all trajectories in the virtual tube are supposed to be the same, which prevents further optimization of total time. To overcome this

problem, in this section, the trajectory in the optimal virtual tube is parameterized by piece-wise continuous Bézier curves. The convex hull property of Bézier curves can remain the trajectory within the convex hull of control points, which guarantees safety. Subsequently, a spatial-temporal trajectory optimization problem based on multi-parametric programming is proposed to improve computational efficiency and passing-through efficiency.

We parameterize a trajectory, denoted as $\mathbf{h}\left(\left(\mathbf{q}_0, \mathbf{q}_1\right), t\right)$, spanning from the start point $\mathbf{q}_0$ to the goal point $\mathbf{q}_1$, as a p-degree piece-wise continuous Bézier curve. Specifically, $\mathbf{h}\left(\mathbf{q}_0, \mathbf{q}_1, t\right)$ is a concatenation of a sequence of $M \in \mathbb{N}$ segments, $\mathbf{h}_1\left(t\right), \mathbf{h}_2\left(t\right), ..., \mathbf{h}_M\left(t\right)$. For segment $m \in \{1, 2, ..., M\}$, $\mathbf{h}_m\left(t\right)$ is characterized by control points $\mathbf{P}_m = \begin{bmatrix} \mathbf{p}_{m,0} & \mathbf{p}_{m,2} & \cdots & \mathbf{p}_{m,p} \end{bmatrix} \in \mathbb{R}^{3 \times (p+1)}$ and duration $\Delta t_m > 0$. Therefore, the whole trajectory $\mathbf{h}\left(\left(\mathbf{q}_0, \mathbf{q}_1\right), t\right)$ could be expressed as

$$\mathbf{h}\left(\left(\mathbf{q}_0, \mathbf{q}_1\right), t\right) \triangleq \mathbf{h}_m\left(t - \sum_{j=1}^{m-1} \Delta t_j\right), \quad (11)$$

where $t \in \left[\sum_{j=1}^{m-1} \Delta t_j, \sum_{j=1}^{m} \Delta t_j\right]$, $\mathbf{q}_0 = \mathbf{p}_{1,0}$. $\mathbf{q}_1 = \mathbf{p}_{M,p}$,

$$\mathbf{h}_m\left(t - \sum_{j=1}^{m-1} \Delta t_j\right) = \mathbf{C}_m \boldsymbol{\beta}^{\mathrm{T}}\left(t\right),$$

$\boldsymbol{\beta}\left(t\right) = \left[1, t, t^2, ..., t^p\right], t \in [0, \Delta t_m], \mathbf{C}_m^{\mathrm{T}} = \mathbf{S}_{\Delta t_m} \mathbf{M} \mathbf{P}_m^{\mathrm{T}}$.

The trajectory $\mathbf{h}\left(\left(\mathbf{q}_0, \mathbf{q}_1\right), t\right)$, or called $\mathbf{h}\left(t\right)$ for simply, is constrained in a sequence of intersected spheres given by Section V-A. The terminals for every segment of the trajectory are placed in the intersection areas of adjoint spheres. This ensures that each segment is confined within distinct spheres, as illustrated in Fig. 7. Consequently, the avoidance constraints can be expressed as:

$$S_m\left(\mathbf{h}_m\left(t\right)\right) \leq 0, m \in 1, ..., M. \quad (12)$$

Together with dynamic feasibility in the form of the derivatives of the trajectory, the spatial-temporal trajectory optimization is formulated by

$$\min_{\mathbf{P}, \mathbf{t}} \int_0^{\sum_{m=1}^{M} \Delta t_m} \left\|\mathbf{h}^{(d)}\left(t\right)\right\|^2 \mathrm{d}t + \rho_t \sum_{m=1}^{M} \Delta t_m \quad (13\mathrm{a})$$

$$\text{s.t. } \mathbf{h}^{[d-1]}\left(0\right) = \bar{\mathbf{p}}_{1,0}, \mathbf{h}^{[d-1]}\left(\sum_{m=1}^{M} \Delta t_m\right) = \bar{\mathbf{p}}_{M,p}, \quad (13\mathrm{b})$$

$$\mathbf{h}_m^{[d-1]}\left(\Delta t_m\right) = \mathbf{h}_{m+1}^{[d-1]}\left(0\right), \quad (13\mathrm{c})$$

$$-\mathbf{i}_m \leq \mathbf{h}_m^{[d-1]}\left(t\right) \leq \mathbf{i}_m, \quad (13\mathrm{d})$$

$$S_m\left(\mathbf{h}_m\left(t\right)\right) \leq 0, \quad (13\mathrm{e})$$

$$m = 1, 2, ..., M, t \in [0, \Delta t_m], \quad (13\mathrm{f})$$

where $\rho_t > 0$ is the weight coefficient, $\mathbf{h}_m^{[d-1]}\left(t\right) = \left[\mathbf{h}_m\left(t\right)^{\mathrm{T}}, \mathbf{h}_m^{(1)}\left(t\right)^{\mathrm{T}}, ..., \mathbf{h}_m^{(d-1)}\left(t\right)^{\mathrm{T}}\right]^{\mathrm{T}}$, $\bar{\mathbf{p}}_{1,0}, \bar{\mathbf{p}}_{M,p}$ are start and goal states up to $(d-1)$-order derivatives, $\mathbf{i}_m$ is the dynamic bounds.

All trajectories within the optimal virtual tube are derived from optimal variables obtained through (13). However, directly solving this problem is highly challenging, and solving infinite optimization problems involving an infinite number of trajectories within the optimal virtual tube is infeasible. To streamline the programming associated with (13), it is decomposed into two distinct steps. In the first step, path points are generated through spatial trajectory optimization, ensuring trajectories remain within the virtual tube and minimizing control efforts, capitalizing on the convex hull property of the Bézier curve. In the second step, feasible dynamics of robots are considered in the temporal trajectory optimization. Subsequently, we employ multi-parametric programming to obtain an infinite set of optimal trajectories by solving a finite number of programmings.

1) Spatial Trajectory Optimization: The boundary trajectories of the virtual tube are generated first. Before formulating the spatial trajectory optimization, a suitable terminal path points selection strategy is designed in this section to make the trajectory in the spheres. As shown in Fig. 7, terminal path points $\mathbf{p}_{m,0}, \mathbf{p}_{m,p}$ for any segment m of the trajectory are constrained within the intersection areas of adjoint spheres to maintain trajectory in free space. Suppose there is a sequence of intersected spheres centered in $\mathbf{o}_m$ with radius r_m $(m = 1, ..., M)$. The intersection area of adjoint spheres centered in $\mathbf{o}_m$ and $\mathbf{o}_{m+1}$ respectively is denoted by $\mathcal{I}_m$. Let $^k\mathbf{p}_{1,0} \in \mathcal{I}_1$ $(k \in 1, 2, ..., k_c)$ be the start point, where k_c is the number of boundary trajectories and is designed manually. Then, other start points in $\mathcal{I}_m$ are expressed as $^k\mathbf{p}_{m,0} \in \mathcal{I}_m$.

To initialize the time allocation $\{\Delta t_m\}$ by the chord length parameterization method [42], the initial positions of terminal points are needed. For convenience, the initial terminal points are set in the maximum intersection plane $\mathcal{I}_{m,\max}$ in the intersection area of adjoint spheres $\mathcal{I}_m$. The $\mathcal{I}_{m,\max}$ is expressed as

$$\mathcal{I}_{m,\max}\left(\rho, \varphi\right) = \mathbf{p}_{o,m} + \rho \lambda_m \left(\mathbf{n}_{o,m} \cos \varphi + \mathbf{b}_{o,m} \sin \varphi\right), \quad (14)$$

where $\varphi \in [0, 2\pi]$, $\rho \in [0, 1]$, $\mathbf{v}_{o,m}$, $\mathbf{n}_{o,m}$ and $\mathbf{b}_{o,m}$ are the unit tangent vector, unit normal vector and unit abnormal vector of the line $\overline{\mathbf{o}_{m+1}\mathbf{o}_m}$ respectively,

$$\mathbf{p}_{o,m} = \mathbf{o}_m + \frac{r_{m+1}^2 - r_m^2 + \left\|\mathbf{o}_{m+1} - \mathbf{o}_m\right\|^2}{2 \left\|\mathbf{o}_{m+1} - \mathbf{o}_m\right\|} \mathbf{v}_{o,m},$$

$$\lambda_m = \sqrt{r_{m+1}^2 - \frac{r_{m+1}^2 - r_m^2 + \left\|\mathbf{o}_{m+1} - \mathbf{o}_m\right\|^2}{2 \left\|\mathbf{o}_{m+1} - \mathbf{o}_m\right\|}}.$$

After that, the time allocations $\{\Delta t_m\}$ for all boundary trajectories are set as the same by the arithmetic mean [43].

Subsequently, the spatial trajectory optimization for a tra-
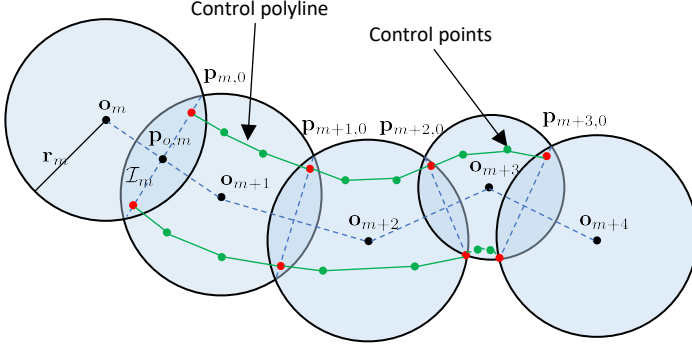
Fig. 7: Examples of spatial trajectory optimization. The red points and green points represent control points. Red points, especially, are terminals of segments that are fixed in the intersection areas of adjoint spheres. The green lines are the control polylines.
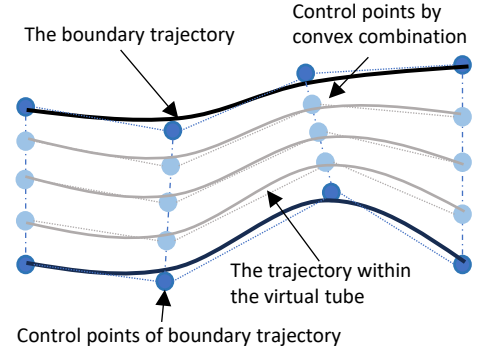

Fig. 8: A method to generate the trajectories within the virtual tube. The dark blue circles and light blue circles represent the control points of boundary trajectories and control points of trajectories within the virtual tube, respectively. The black curves are boundary trajectories, and the gray curves are trajectories within the virtual tube.

jectory $\mathbf{h}(t)$ in the virtual tube is formulated by

$$\min_{\mathbf{P}} \int_0^{\sum_{m=1}^M \Delta t_m} \left\| \mathbf{h}^{(d)}(t) \right\|^2 dt \tag{15a}$$

$$\text{s.t.} \mathbf{h}^{[d-1]}(0) = \bar{\mathbf{p}}_{1,0}, \mathbf{h}^{[d-1]}\left(\sum_{m=1}^M \Delta t_m\right) = \bar{\mathbf{p}}_{M,p}, \tag{15b}$$

$$\mathbf{h}_m^{[d-1]}(\Delta t_m) = \mathbf{h}_{m+1}^{[d-1]}(0), \tag{15c}$$

$$S_m(\mathbf{h}_m(t)) \le 0, \tag{15d}$$

$$-\mathbf{i}_m \le \mathbf{h}_i^{[d-1]}(t) \le \mathbf{i}_m, \tag{15e}$$

$$m = 1, 2, ..., M, t \in [0, \Delta t_m]. \tag{15f}$$

Thus, the k_c boundary trajectories can be generated by (15). And for any trajectory $\mathbf{h}_{\boldsymbol{\eta}}(t)$ in the virtual tube whose start point is

$$\mathbf{p}_{1,0}(\boldsymbol{\eta}) = \sum_{k=1}^{k_c} \eta_k {}^k\mathbf{p}_{1,0}, \sum_{k=1}^{k_c} \eta_k = 1, \eta_k \ge 0,$$

according to *Lemma 2* in [2], the control points of any segment m of trajectory $\mathbf{h}_{\boldsymbol{\eta}}(t)$ generated by (15) are expressed as

$$\mathbf{P}_m(\boldsymbol{\eta}) = \sum_{k=1}^{k_c} \eta_k {}^k\mathbf{P}_m, \sum_{k=1}^{k_c} \eta_k = 1, \eta_k \ge 0. \tag{16}$$

According to (16), control points for any trajectory in the virtual tube are expressed as the convex combination of control points of boundary trajectories, as shown in Fig. 8.

2) Temporal Trajectory Optimization: The control points of the boundary trajectories are generated by the above subsection. The object of the temporal trajectory optimization problem is to arrive at a goal as fast as possible, in other words, to minimize the total time. Thus, the optimization problem is expressed as

$$\min_{\mathbf{t}} \sum_{m=1}^M \Delta t_m \tag{17a}$$

$$\text{s.t.} -\mathbf{i}_m \le \mathbf{h}_m^{[d-1]}(t) \le \mathbf{i}_m, \tag{17b}$$

$$\mathbf{h}_m^{[d-1]}(\Delta t_m) = \mathbf{h}_{m+1}^{[d-1]}(0), \tag{17c}$$

$$m = 1, 2, ..., M, t \in [0, \Delta t_m]. \tag{17d}$$

In this problem, because of the mass point model of the robot in (6), we only constrain the velocity so that the problem (17) is transformed into a linear programming:

$$\min_{\mathbf{t}} \sum_{m=1}^M \Delta t_m \tag{18a}$$

$$\text{s.t.} -\mathbf{v}_m \le \frac{p}{\Delta t_m}(\mathbf{p}_{m,k+1} - \mathbf{p}_{m,k}) \le \mathbf{v}_m \tag{18b}$$

$$\frac{(\mathbf{p}_{m,p} - \mathbf{p}_{m,p-1})}{\Delta t_m} = \frac{(\mathbf{p}_{m+1,1} - \mathbf{p}_{m+1,0})}{\Delta t_{m+1}}, \tag{18c}$$

$$\Delta t_m > 0, m = 1, 2, ..., M, k = 0, ..., p-1. \tag{18d}$$

where $\mathbf{v}_m$ are the velocity limitations of the robot. Thus, (18) could be expressed as the standard form, which is expressed as

$$\min_{\mathbf{x}} \mathbf{c}^T\mathbf{x} \tag{19}$$
$$\text{s.t.} \mathbf{A}\mathbf{x} \le \mathbf{b},$$

where $\mathbf{x} = [\Delta t_1 \ \Delta t_2 \ \cdots \ \Delta t_M]^T$, $\mathbf{A}$ is a matrix with respect to $\mathbf{v}_m$ and $\mathbf{p}_{m,k}$, and $\mathbf{b}$ is linear with $\mathbf{p}_{m,k}$.

Because there are k_c boundary trajectories in the virtual tube. The optimization problem of the k-th boundary trajectory $\mathbf{h}_k(t)$ is expressed as

$$\min_{\mathbf{x}} \mathbf{c}^T\mathbf{x} \tag{20}$$
$$\text{s.t.} \mathbf{A}_k\mathbf{x} \le \mathbf{b}_k.$$

For any trajectory $\mathbf{h}_{\boldsymbol{\theta}}(t)$ within the virtual tube, the control points are the convex combination of the control points of the boundary trajectories, namely $\mathbf{P}_{\boldsymbol{\theta}} \in \text{conv}\left(\{{}^k\mathbf{P}\}\right)$. Thus, the optimization problem of the trajectory $\mathbf{h}_{\boldsymbol{\theta}}(t)$ is expressed as

$$\min_{\mathbf{x}} \mathbf{c}^T\mathbf{x} \tag{21}$$
$$\text{s.t.} \mathbf{A}(\boldsymbol{\theta})\mathbf{x} \le \mathbf{b}_1 + \mathbf{F}\boldsymbol{\theta},$$

where $\mathbf{F} = [\mathbf{b}_2 - \mathbf{b}_1 \ \cdots \ \mathbf{b}_{k_c} - \mathbf{b}_1]$, $\mathbf{A}(\boldsymbol{\theta}) = \mathbf{A}_1 + \sum_{k=1}^{k_c-1} \theta_k \mathbf{A}_{k+1}$, $\boldsymbol{\theta} = [\theta_1 \ \theta_2 \ \cdots \ \theta_{k_c-1}]^T$, $\sum_{k=1}^{k_c-1} \theta_k = 1$, $\theta_k \ge 0$. The optimal value of (21) is denoted as $V^*(\boldsymbol{\theta})$.

Because the domain of $\boldsymbol{\theta}$ is bounded and continuous, it is impossible to directly solve for the optimal solutions corresponding to all $\boldsymbol{\theta}$. A recursive algorithm, detailed in *Algorithm 1*, for approximate multi-parametric programming [44] could be used to find the critical regions CR_θ for all $\boldsymbol{\theta}$ and the corresponding explicit optimal solutions $\mathbf{x}^*_{CR_\theta}(\boldsymbol{\theta}) = \mathbf{X}\mathbf{M}^{-1}[1\ \boldsymbol{\theta}]^{\mathrm{T}}$ within the error bound ϵ, where $\mathbf{X}$ and $\mathbf{M}$ are related to the corresponding region in CR_θ. Therefore, if the trajectory

---

Algorithm 1 An approximate multi-parametric programming

Input: (i) parameter vectors $\boldsymbol{\theta}_1, \boldsymbol{\theta}_2, ..., \boldsymbol{\theta}_{k_c-1} \in CR_\theta$; (ii) the optimal values $\mathbf{v}_{\mathrm{opt}} = [V^*(\boldsymbol{\theta}_1), V^*(\boldsymbol{\theta}_2), ..., V^*(\boldsymbol{\theta}_{k_c-1})]$ of (21) corresponding to the parameter vectors; (iii) vector $\mathbf{x}^*_1, \mathbf{x}^*_2, ..., \mathbf{x}^*_{k_c-1}$ such that $\mathbf{x}^*_k$ is the optimal solution of (21) for all $k = 1, 2, ..., k_c - 1$; (iv) the error bound ϵ.
Output: the parameters $\mathbf{M}$ and $\mathbf{X}$ corresponding to the critical regions CR_θ.

1: Build $\mathbf{M} = \begin{bmatrix} 1 & 1 & \cdots & 1 \\ \boldsymbol{\theta}_1 & \boldsymbol{\theta}_2 & \cdots & \boldsymbol{\theta}_{k_c-1} \end{bmatrix}$;
2: Build $\mathbf{X} = \begin{bmatrix} \mathbf{x}^*_1 & \mathbf{x}^*_2 & \cdots & \mathbf{x}^*_{k_c-1} \end{bmatrix}$;
3: **if** M is nonsingular **then**
4:    Compute the optimum $\tilde{\epsilon}$ and an optimizer $(\bar{\mathbf{x}}, \bar{\boldsymbol{\theta}})$ of

$$\max_{\mathbf{x},\boldsymbol{\theta}} \quad V(\boldsymbol{\theta}) - \mathbf{c}^{\mathrm{T}}\mathbf{x}$$
$$\text{s.t.} \quad \mathbf{A}(\boldsymbol{\theta})\mathbf{x} \leq \mathbf{b}_1 + \boldsymbol{F}\boldsymbol{\theta}$$
$$\mathbf{M}^{-1}\begin{bmatrix} 1 \\ \boldsymbol{\theta} \end{bmatrix} \geq 0,$$
$$\text{where } V(\boldsymbol{\theta}) = \mathbf{v}_{\mathrm{opt}}\mathbf{M}^{-1}\begin{bmatrix} 1 \\ \boldsymbol{\theta} \end{bmatrix};$$

5:    **if** $\tilde{\epsilon} > \epsilon$ **then**
6:       **for** $k = 1, 2, ..., k_c - 1$ **do**
7:          replace $\boldsymbol{\theta}_k$ by $\bar{\boldsymbol{\theta}}$, $V^*(\boldsymbol{\theta}_k)$ by $V(\bar{\boldsymbol{\theta}})$, and $\mathbf{x}^*_k$ by $\bar{\mathbf{x}}$;
8:          call this algorithm;
9:       **end for**
10:    **else**
11:       **return** $(\mathbf{M}, \mathbf{X})$
12:    **end if**
13: **end if**

$\mathbf{h}^*_{\boldsymbol{\theta}}(t)$ in which

$$\mathbf{P} = \sum_{k=1}^{k_c} \theta_k \mathbf{P}_k \in \mathrm{conv}(\{\mathbf{P}_k\}), \mathbf{t} = \mathbf{x}^*_{CR_\theta}(\boldsymbol{\theta}), \quad (22)$$

the trajectory $\mathbf{h}^*_{\boldsymbol{\theta}}(t)$ is optimal.

C. Complexity Analysis

In this subsection, the computational complexity of the traditional trajectory planning method is first analyzed, followed by that of the proposed method. Subsequently, a comparative analysis is conducted to highlight the differences in computational complexity between the two methods.

The traditional trajectory planning method formulates an optimization problem by treating trajectory parameters as optimization variables and solving for the optimal trajectory. Accordingly, the computational complexity of generating a single trajectory is $O(n_t^3)$, and the computational complexity of generating k trajectories is $O(kn_t^3)$, where n_t denotes the number of optimization variables.

The computational complexity of the trajectory planning method proposed in this paper can be divided into two parts: critical region generation and trajectory generation. As shown in *Algorithm 1*, the critical regions are generated recursively, so its computational complexity depends not only on the number of optimization variables n_t but also on the number of boundary trajectories k_c and the number of regions λ resulting from the partitioning of the critical regions [44]. Consequently, the computational complexity of critical region generation can be expressed as $O(\lambda(n_t + k_c)^3)$. For trajectory generation, the process involves first locating the corresponding regions within the critical regions and then generating the k trajectory through affine functions. Thus, the computational complexity of this process is $O(kn_t)$, where n_t denotes the number of optimization variables. In summary, the total computational complexity of the proposed method for generating k trajectories can be expressed as $O(\lambda(n_t + k_c)^3 + kn_t)$, where n_t is the number of optimization variables and k_c is the number of boundary trajectories with respect to $\boldsymbol{\theta}$ for multi-parametric programming.

Compared to the computational complexity of the traditional method, the proposed method introduces the additional complexity of critical region generation. However, the computational complexity of trajectory generation is reduced from $O(n_t^3)$ to $O(n_t)$. More interestingly, the computational complexity of critical region generation is independent of the number of trajectories k. This leads to the result that the number of trajectories generated has a negligible impact on the computational cost of the proposed method. As the number of trajectories increases, the computational advantage of the proposed method becomes more pronounced.

VI. CONTROLLER

The controller combining trajectory tracking and collision avoidance is described in the following. Suppose the parameters of the trajectory for the robot i to track are $\boldsymbol{\theta}_i$. Then, according to (22) and (4), the optimal trajectory $\mathbf{h}^*_{\boldsymbol{\theta}_i}(t)$ is generated by affine functions which have a low computational complexity.

The controller shown in Fig. 9 refers to the work in virtual tube control problem [29], which can be expressed as

$$\mathbf{v}_{c,i} = \mathbf{v}_{t,i} + \mathbf{v}_{b,i} + \mathbf{v}_{a,i},$$

where $\mathbf{v}_{c,i}$ is the velocity command for robot i in (6), $\mathbf{v}_{t,i} = \frac{\mathrm{d}\mathbf{h}^*_{\boldsymbol{\theta}_i}(t)}{\mathrm{d}t}$ is the feedforward velocity from the trajectory, $\mathbf{v}_{b,i}$ is the command to track the trajectory and $\mathbf{v}_{a,i}$ is the avoidance command to avoid the collision with other robots. By integrating feedforward, tracking, and avoidance commands, the controller enables the robot to track the planned trajectory while ensuring safety and avoiding collisions.
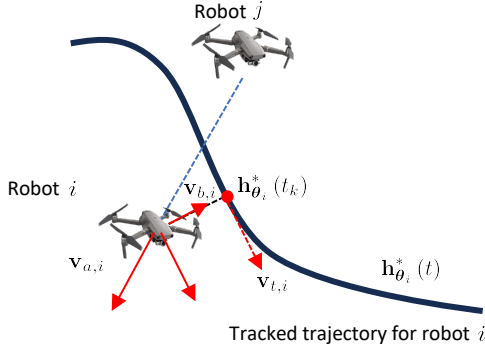
Fig. 9: The controller for the robot i in the swarm. The black curve represents the optimal trajectory tracked by the robot i. The red point denotes the corresponding point $\mathbf{h}^*_{\boldsymbol{\theta}_i}(t_k)$ in the trajectory $\mathbf{h}^*_{\boldsymbol{\theta}_i}(t)$ to the robot i. And, the three vectors represent feedforward command $\mathbf{v}_{t,i}$, tracking command $\mathbf{v}_{b,i}$, and avoidance command $\mathbf{v}_{a,i}$ respectively, in which the feedforward command $\mathbf{v}_{t,i}$ is the tangent vector of the point $\mathbf{h}^*_{\boldsymbol{\theta}_i}(t_k)$ and the avoidance command $\mathbf{v}_{a,i}$ is align with the line between robot i and robot j.

Remark 1. *The details of the stability proof for the controller, as well as the specific formulations of $\mathbf{v}_{b,i}$ and $\mathbf{v}_{a,i}$, can be found in the relevant proof in [29].*

VII. SIMULATIONS AND EXPERIMENTS

In this section, the theoretical effectiveness of the proposed method is first validated through numerical experiments. Then, its advantages in flight safety and efficiency are demonstrated through flight simulations. Next, hardware-in-the-loop (HIL) simulations are performed to compare the proposed method with a traditional trajectory optimization method named EGO-swarm [23], showcasing the computational efficiency and real-time performance of the proposed method. Finally, swarm flight experiments in unknown environments are implemented to evaluate and validate the real-time performance and effectiveness of the proposed method.

A. Simulations and Experiments Setup

The numerical experiments for theoretical validation and flight simulations are conducted on a PC with a CPU i9-13900KF and 32GB RAM, using MATLAB for coding. The 3-D obstacle environment, shown in Fig. 10, is $250 \times 200 \times 30$m, and the size of the random obstacles is $10 \times 10 \times 30$m.

For HIL simulation to verify the real-time performance and the computational efficiency of the proposed method, the platform includes drones shown in Fig. 11 and RflySim [45] simulator shown in Fig 12. The drone is equipped with a LiDAR (MID-360), a flight controller, and an onboard computer (NVIDIA Jetson Orin). The code is written in C++ and runs on the Ubuntu 20.04 OS. The solver used in the proposed method is MOSEK.

For the real flight experiments, drones identical to those used in the HIL simulations are employed. The LiDAR is used for autonomous localization and generates the point
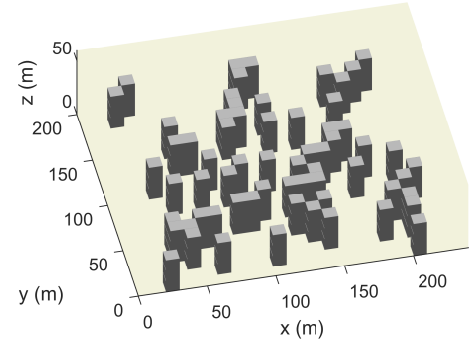

Fig. 10: The 3-D environment with random obstacles used for comparative validations.
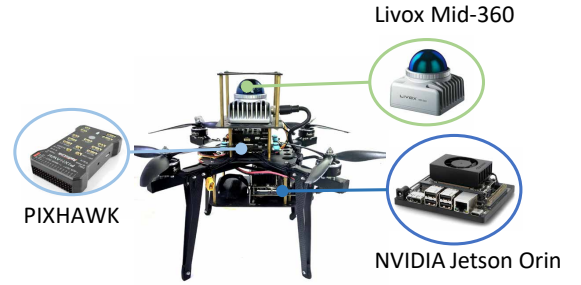

Fig. 11: The drone is used for HIL simulations and real flight experiments.

cloud map for swarm trajectory planning and control. Inter-drone communication is implemented via WiFi. The unknown obstacle environments are shown in Fig. 13, with obstacles randomly placed. The drone swarm takes off from the start area, navigates through the obstacle environment, and reaches the goal area. The safety distance between drones is 0.8m. The number of drones in the swarm is 3.

B. Numerical Validation

In this subsection, the process of optimal virtual tube planning is briefly described. Subsequently, the theoretical effectiveness of the proposed planning method is validated, while the effects of the error bound ϵ of the proposed method on the approximation results are investigated.
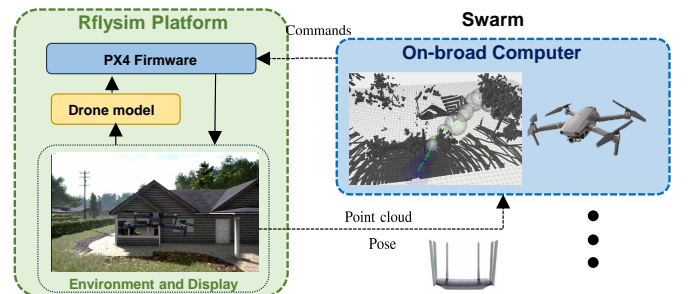

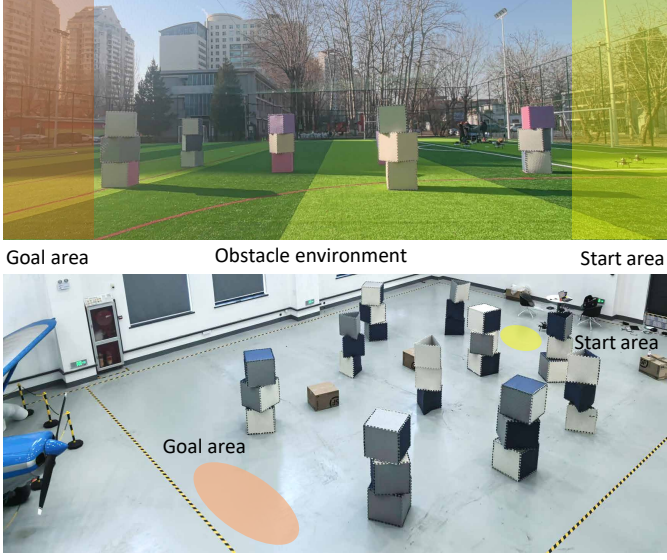Fig. 12: The hard-in-the-loop (HIL) simulation platform.

Fig. 13: The unknown environments with random obstacles. The blue and red blocks represent the start and goal areas, respectively.

The 3-D obstacle environment is shown in Fig. 14(a). With fixed start and goal regions, the homotopic paths in the same homotopy class are planned by [3], as depicted in Fig. 14(b). Based on the homotopic paths, the optimal virtual tube planning is then divided into two steps: spatial trajectory planning and temporal trajectory planning. The step of spatial trajectory planning, illustrated in Fig. 14(c), generates an infinite set of optimal trajectories with initial time allocations. The step of temporal trajectory planning, shown in Fig. 14(d), generates the optimal time allocations for all trajectories in the infinite set of trajectories.

In Step 3, for any trajectory in the infinite set of spatial trajectories, the control points can be approximated by the convex combination of control points of boundary trajectories [2]. However, in Step 3, all trajectories use the same initial time allocations. Therefore, in Step 4, the time allocations for all trajectories are optimized. Here, the critical regions are generated by *Algorithm 1*, as shown in Fig. 14(d.1). Any trajectory can be mapped to a specific region within the critical regions, and the optimal time allocations for that trajectory can be linearly approximated using the three vertices of the corresponding region. To numerically validate this method, hundreds of points are uniformly sampled within the critical regions. The true optimal values and their approximations are then computed under different error bounds ϵ, as shown in Fig. 14(d.2). As demonstrated in Fig. 14(d.3), the proposed method successfully approximates the optimal values within the specified error bound ϵ. For a more intuitive representation, the critical regions are visually mapped onto the trajectories, as illustrated in Fig. 14(d.4).

C. Flight Simulations

In this subsection, the performance of the drone swarm within the optimal virtual tube is validated in the same environment. The obstacle environment and the parameter settings of the optimal virtual tube are consistent with those in the previous subsection. The drone swarm consists of 36 drones, with the radius r_s of the safety area set to 0.4m and the radius r_a of the avoidance area set to 1m. The time trajectory planning uses the results from the initial time interval as well as $\epsilon = 0.8$.

The trajectory results of the swarm are shown in Fig. 15, where different colors along the trajectories represent different time stamps. A comparison of the trajectories reveals differences in time allocations between the various optimal trajectories. As shown in Fig. 16(a), the swarm with approximate temporal trajectory planning reaches the goal area faster and in a shorter time. This observation is further corroborated by the speed and inter-drone distance data, as shown in Fig. 16. From Fig. 16(a), it can be observed that the swarm with approximate temporal trajectory planning reaches the goal area faster and in a shorter time. In the initial time allocation, the high number of drones in the swarm leads to unsafe distances in narrower areas, as depicted in Fig. 16(b). Additionally, the inter-drone safety distance is larger when the swarm is more dispersed, in contrast to the swarm with the initial time allocations. This further emphasizes the influence of temporal trajectory planning on both swarm speed and safety.

D. Numerical Analysis of Computation Time

The efficient computation time of the proposed method is compared with the traditional method from two aspects: one is the effect of different replanning frequencies on the computational time, and the other is the effect of the number of trajectories on the total computational time. All simulations are conducted on the hardware platform to maintain consistency with the real-world experiments. Meanwhile, due to the differences in the framework of the proposed method and the traditional method, two metrics are adopted for comparison: individual computation time and total computation time. The former refers to the computation time required for each robot, while the latter denotes the sum of the computation times of all robots in the swarm.

To analyze the effect of replanning frequency on computation time, the HIL simulations with three drones are implemented on the RflySim platform. The same start and goal areas are set where the drones navigate through a forested environment, as shown in Fig. 17(a). Different views of the swarm trajectories for the two methods are illustrated in Fig. 17(b) and Fig. 17(c). The computation times of two methods in different frequencies are listed in Table I. In Table I, since the proposed method is a centralized trajectory planning approach, it is necessary to distinguish between the individual computation time of the host drone and that of the other drones. From the computation times in Table I, it can be observed that as the replanning frequency increases, the computation times for both methods increase. Although the individual computation time for the host drone in our method is consistently higher, the total computation time remains smaller due to the very low computation times of the other drones. Additionally, it can be seen that, due to the minimal
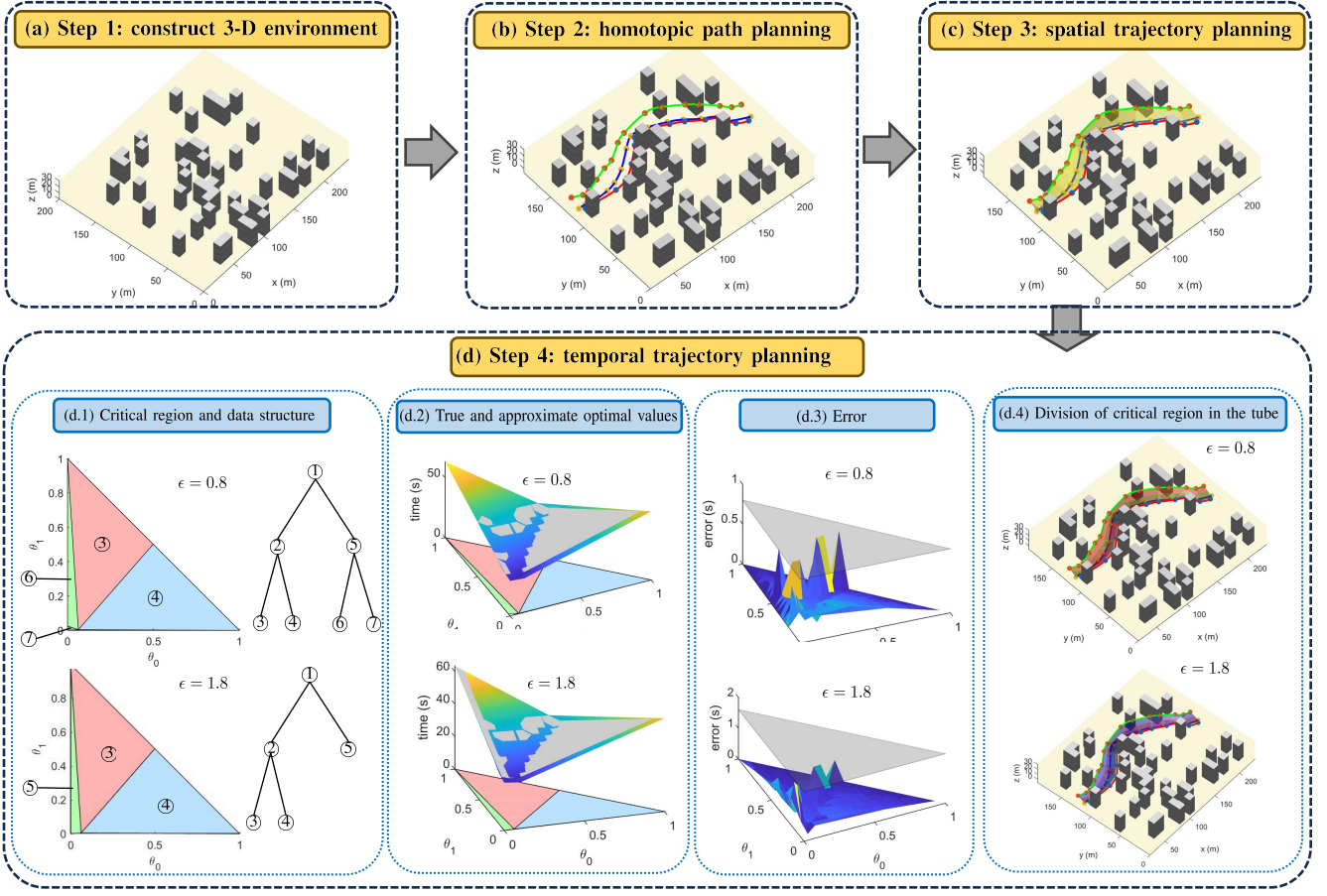
Fig. 14: The process and validation of optimal virtual tube planning. (a) A random obstacle environment in 3-D space is constructed. (b) The homotopic paths denoted by the colorful curves are generated by the Tube RRT* algorithm. (c) The infinite set of spatial trajectories is represented by the yellow area among the boundary trajectories. (d.1) The different colors of triangles represent the different regions in critical regions. The data of the critical regions is stored in a tree structure. (d.2) The gray surfaces represent the approximate optimal values by multi-parametric programming, and the colorful surfaces represent the true optimal values by trajectory planning. (d.3) The gray surface represents the error bound ϵ, and the colorful surface represents the error between the approximate and true optimal values. (d.4) The different colors represent the different regions divided by the critical regions in the optimal virtual tube.
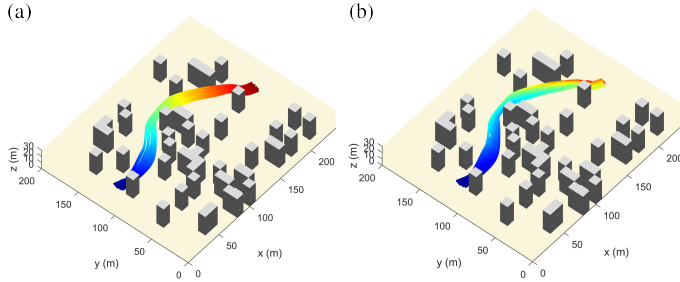

Fig. 15: The trajectories of swarm with different time allocations. The different colors of the trajectories correspond to different time stamps. (a) Results for initial time allocations. (b) Approximate time allocations with $\epsilon = 0.8$.

computation time for the calculations, the effect of replanning frequency on the individual computation time of the other drones can be considered negligible.
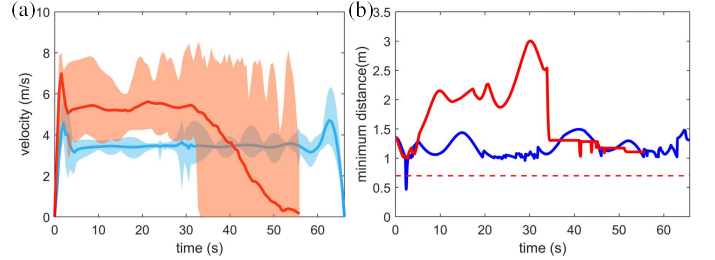

Fig. 16: Speed distribution and the minimum distance among drones. (a) Speed distribution of the swarm: The orange and blue areas show the speed range for $\epsilon = 0.8$ and the initial time allocations, while the red and blue curves represent the corresponding average speed. (b) The minimum distance among the swarm: The red and blue curves represent the minimum distance among drones for $\epsilon = 0.8$ and the initial time allocations, respectively. And the red dotted line represents the safety distance between two drones.

(a) Forest environment in RflySim (b) EGO-swarm (c) The proposed method
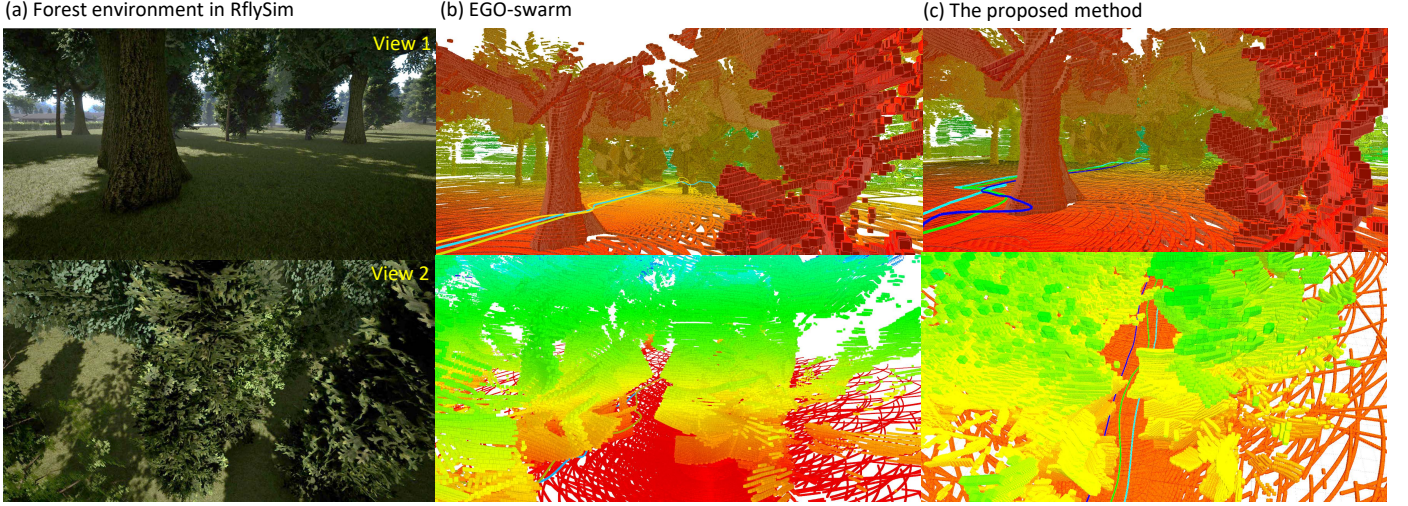

Fig. 17: The results of trajectories for two methods in HIL. Different colors of curves represent the different trajectories of drones in the swarm. (a) The forest environment in the simulator. (b) Trajectories generated by EGO-swarm. (b) Trajectories generated by the proposed method.

Replan Frequency (Hz)		1	2	5	10
Computation time (s)	EGO-swarm	—$|$0.009$|$0.029	—$|$0.013$|$0.037	—$|$0.031$|$0.094	—$|$0.047$|$0.141
	Ours	0.015$|$0.92 $\times$ 10^{-6} $|$0.015	0.021$|$2.64 $\times$ 10^{-6}$\|$0.021	0.082$\|$5.83 $\times$ 10^{-6}$|$0.082	0.117$|$1.29 $\times$ 10^{-5}$|$0.117

TABLE I: Comparison of computation time at different frequencies: EGO-swarm versus Ours. The individual computation time for the host drone and other drones and the total computation time at each frequency for each method are separated by vertical bars.

The total computation times for both the traditional method and the proposed method, under varying numbers of trajectories and different error bounds ϵ, are presented in Fig. 18. As observed, the computation time for the traditional method increases with the number of trajectories, while the proposed method is less sensitive to this factor, exhibiting only a slight increase. This minor increase can be attributed to the time required for linear computations, which is significantly shorter than the time needed for optimization solving. Furthermore, the computation time is influenced by the size of the error bound ϵ. Smaller error bounds result in longer computation times, as they lead to higher approximation accuracy, necessitating finer partitioning of critical regions, which slightly increases the total computation time. Overall, the proposed method achieves an order-of-magnitude reduction in computation time compared to traditional methods, remains minimally affected by the number of trajectories, and requires a chosen error bound to balance computational cost and accuracy.

E. Experiment Results

In this subsection, several experiments are implemented to evaluate the proposed method. Initially, comparative experiments are conducted to analyze the effect of obstacle positioning in environments on swarm flight. Subsequently, the experiments in two scenarios including indoor and outdoor environments, as shown in Fig. 20(a) and Fig. 21(a), are implemented to validate the real-time performance of the proposed method.
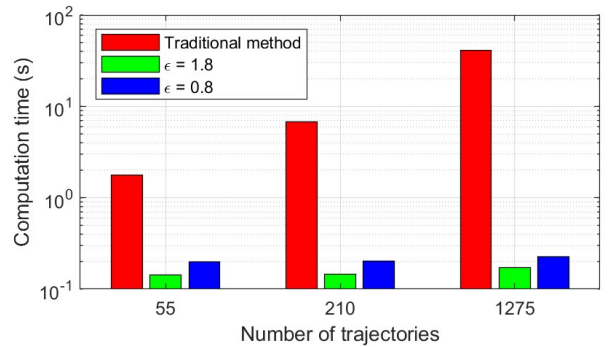

Fig. 18: Computation time vs Number of trajectories. The red, green, and blue blocks represent the total computation times of the traditional method, $\epsilon = 1.8$, and $\epsilon = 0.8$ respectively.

1) Comparative Experiments: The experimental configuration comprises a priori unknown indoor environment, as illustrated in Fig. 19(a). Obstacle spatial constraints were manipulated by dynamically adjusting a moveable obstacle to modulate the gap size. A comparative experiment was conducted pre- and post-obstacle displacement, with the results of swarm trajectories depicted in Fig. 19(b)-(d). Experimental results demonstrate that the centralized trajectory planning framework induces homotopy-equivalent swarm movement patterns, while the implemented homotopy-based path planning algorithm achieves to select the larger gap within the

obstacle environments.

2) Indoor Experiment: For the indoor environment with dense obstacles, the time-varying trajectories, shown in Fig. 20(a)-(b), demonstrate that temporal trajectory planning enables the swarm to stagger their passage through narrow gaps, effectively reducing the risk of collisions. As presented in Fig. 20(c), the maximum flight speed in the dense obstacle environment reached 1.6 m/s, while the minimum inter-drone distance remained above the safety distance of 0.8 m.

3) Outdoor Experiment: In the outdoor environment with sparse obstacles, the time-varying trajectories depicted in Fig. 21(a)-(b) illustrate a similar staggered passage strategy, ensuring safe navigation through obstacles. The swarm achieved a higher maximum speed of 2 m/s in the sparse obstacle environment, as shown in Fig. 21(c), while maintaining a safe inter-drone distance of at least 0.8 m.

These results, which closely align with simulation outcomes, further validate the real-time performance and effectiveness of the proposed method in real-world environments.

F. Discussion

Several key observations can be discussed based on the results from the simulations and the real flight experiments. The proposed centralized trajectory planning method demonstrates advantages over traditional methods of efficient computation, homotopic trajectory planning, and collaboration within the swarm. These advantages not only enhance the performance of the swarm but also provide strong support for real-world applications, particularly in complex environments requiring coordinated tasks.

1) Efficient Computation: The proposed centralized trajectory planning method offers significant computational efficiency compared to traditional methods. Although there is a slight increase in the computation time for the host drone, applying multi-parametric programming with a linear approximation of the optimal solution greatly reduces the computation time for the other drones. This method results in a substantial decrease in the total computation time of the swarm. As the number of drones in the swarm increases, the reduction in computation time becomes more pronounced. Specifically, the centralized method allows for collaborative computation within the swarm and the efficient allocation of resources, ensuring that each robot only performs key calculations at critical moments rather than redundantly solving optimization problems for every task. The proposed method not only improves computational efficiency but also ensures real-time responsiveness, meeting the requirements of practical applications.

2) Homotopy Trajectories: One key advantage of centralized trajectory planning is that it ensures all drones in the swarm follow trajectories within the same homotopy class, as shown in Fig. 17(c). This means that all drones adhere to a unified trajectory planning pattern, ensuring that the trajectories of the swarm maintain topological consistency, unlike distributed trajectory planning where non-homotopic trajectories may emerge, as shown in Fig. 17(b). In specific applications, such as the transportation of payloads for swarms

in complex environments, it is critical for the swarm to maintain coordinated and consistent trajectories to avoid interference between drones. The centralized trajectory planning ensures that the trajectories are synchronized, allowing for more efficient task execution, particularly in tasks requiring precise coordination.

3) Swarm Collaboration: While a distributed planning framework does not require the division of tasks among the agents, a centralized planning framework, where each agent consumes different amounts of computational resources, necessitates a hierarchical framework of the swarm. Although the centralized planning framework makes the swarm structure more complex, it also optimizes the allocation of computational resources. For example, more computational resources can be allocated to the host drone to handle more computations, while other drones can be tasked with specific duties such as swarm localization or sensing and recognition tasks. This hierarchical framework allows for efficient task execution, ensuring that the computational load of each agent is balanced and that the overall swarm operates optimally. By assigning resources based on the importance and complexity of tasks, the swarm can collaborate more efficiently and maximize the utilization of the overall computational resources.

VIII. CONCLUSION AND FUTURE WORK

For autonomous navigation for robot swarms in unknown environments, smooth motion with low computation cost is a significant challenge. This paper is based on multi-parametric programming to generate optimal trajectories with linear computation complexity, greatly enhancing re-planning frequency. Additionally, an update strategy is designed to enable real-time operation in unknown environments. The effectiveness and real-time performance of the method are validated through simulations and experiments. In future work, distributed optimal virtual tube planning in communication-denied environments will be investigated to improve the reliability of its applications.

REFERENCES

[1] B. Şenbaşlar and G. S. Sukhatme, "Asynchronous Real-time Decentralized Multi-robot Trajectory Planning," in *2022 IEEE/RSJ International Conference on Intelligent Robots and Systems (IROS)*. IEEE, 2022, pp. 9972–9979.

[2] P. Mao, R. Fu, and Q. Quan, "Optimal Virtual Tube Planning and Control for Swarm Robotics," *The International Journal of Robotics Research*, vol. 43, no. 5, pp. 602–627, 2024.

[3] P. Mao, S. Lv, and Q. Quan, "Tube-RRT*: Efficient Homotopic Path Planning for Swarm Robotics Passing-Through Large-Scale Obstacle Environments," *IEEE Robotics and Automation Letters*, vol. 10, no. 3, pp. 2247–2254, 2025.

[4] O. Khatib, "Real-time Obstacle Avoidance for Manipulators and Mobile Robots," *The International Journal of Robotics Research*, vol. 5, no. 1, pp. 90–98, 1986.

[5] E. G. Hernández-Martínez, E. Aranda-Bricaire, F. Alkhateeb, E. Maghayreh, and I. Doush, "Convergence and Collision Avoidance in Formation Control: A Survey of the Artificial Potential Functions Approach," *Multi-agent Systems—Modeling, Control, Programming, Simulations and Applications*, pp. 103–126, 2011.

[6] S. M. H. Rostami, A. K. Sangaiah, J. Wang, and X. Liu, "Obstacle Avoidance of Mobile Robots Using Modified Artificial Potential Field Algorithm," *EURASIP Journal on Wireless Communications and Networking*, vol. 2019, no. 1, pp. 1–19, 2019.
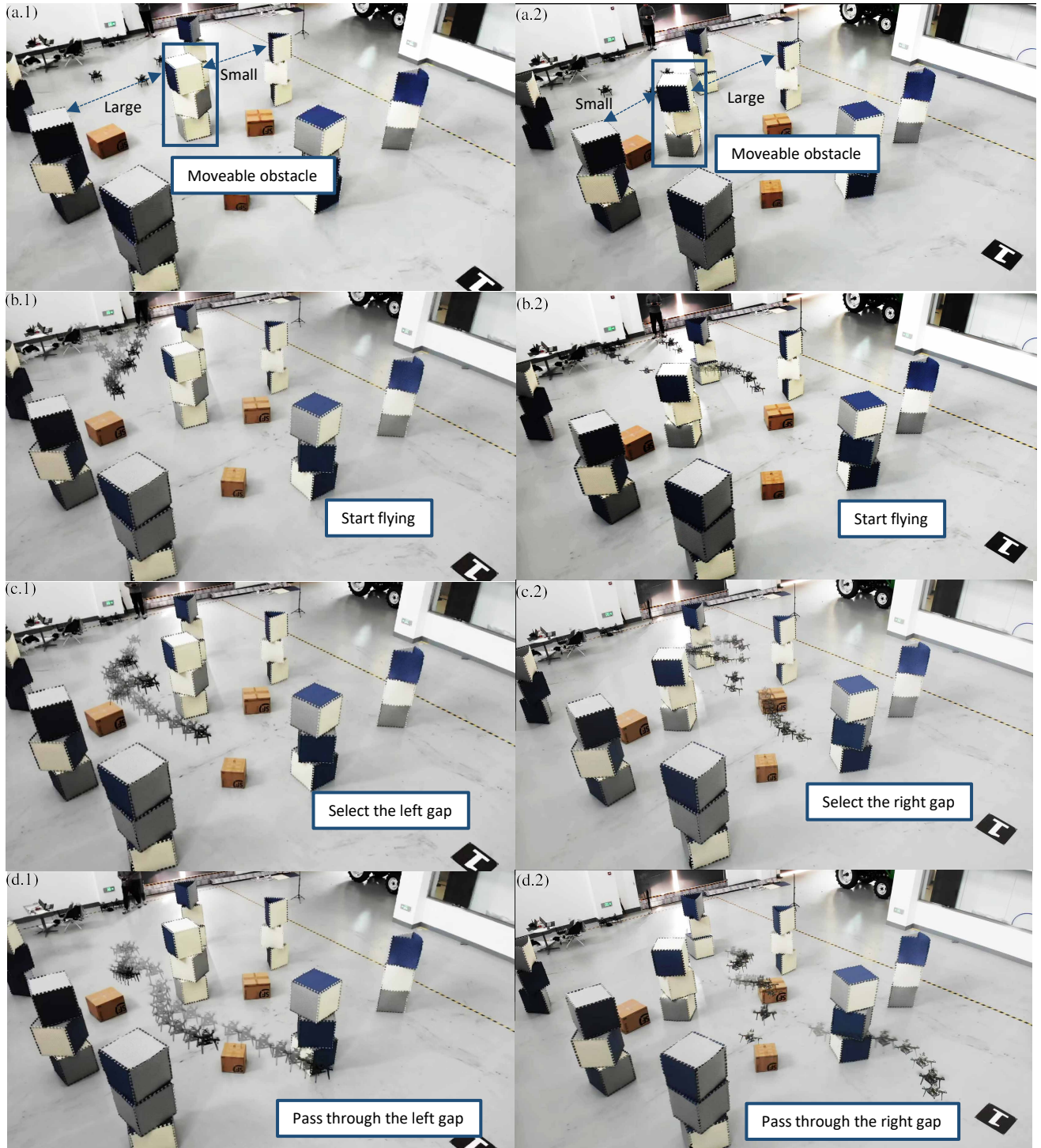
Fig. 19: Comparative experiments in scenario 1 with a moveable obstacle. (a) Obstacle at different positions: in (a.1), the large gap is on the left; in (a.2), the large gap is on the right. (b) Trajectories of the swarm at the start of flight in the respective environments. (c) Trajectories of the swarm as they approach and select the large gap. (d) Trajectories of the swarm passing through the large gap.
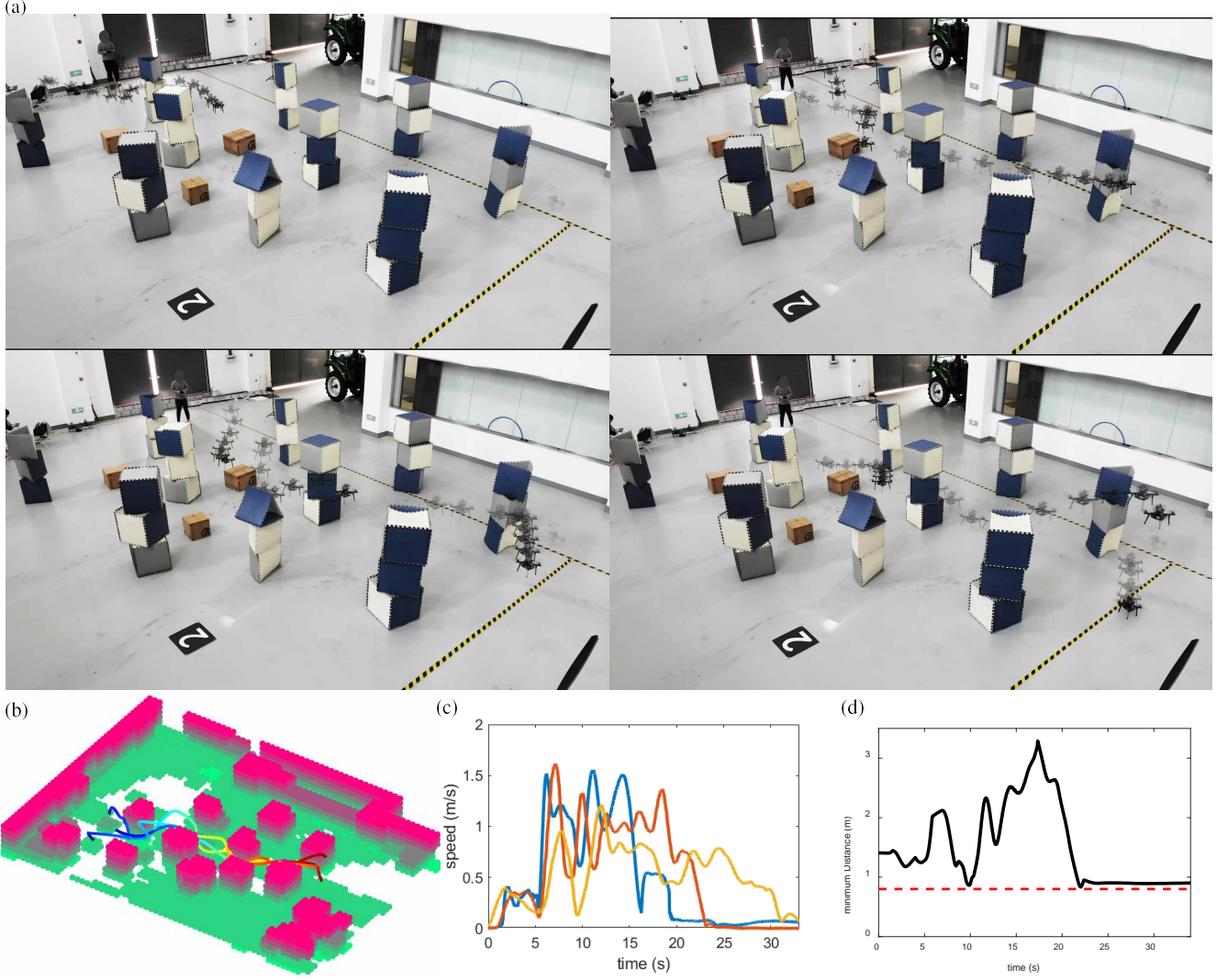
Fig. 20: The real flight experiments in scenario 2. (a) The composite image of drone swarm flight. (b) The swarm trajectories in the point cloud maps. The trajectories at different time stamps are represented in different colors. (c) Swarm speeds and minimum distances among drones over time. The red, yellow, and blue curves represent the speed of drones 0, 1, and 2, respectively. The red dotted line represents the safety distance between drones. The black curve denotes the minimum distance among drones.

[7] J. Antich and A. Ortiz, "Extending the Potential Fields Approach to Avoid Trapping Situations," in *2005 IEEE/RSJ International Conference on Intelligent Robots and Systems*. IEEE, 2005, pp. 1386–1391.

[8] S. S. Ge and C.-H. Fua, "Queues and Artificial Potential Trenches for Multirobot Formations," *IEEE Transactions on Robotics*, vol. 21, no. 4, pp. 646–656, 2005.

[9] A. D. Ames, S. Coogan, M. Egerstedt, G. Notomista, K. Sreenath, and P. Tabuada, "Control Barrier Functions: Theory and Applications," in *2019 18th European control conference (ECC)*. IEEE, 2019, pp. 3420–3431.

[10] A. Singletary, K. Klingebiel, J. Bourne, A. Browning, P. Tokumaru, and A. Ames, "Comparative Analysis of Control Barrier Functions and Artificial Potential Fields for Obstacle Avoidance," in *2021 IEEE/RSJ International Conference on Intelligent Robots and Systems (IROS)*. IEEE, 2021, pp. 8129–8136.

[11] L. Wang, A. D. Ames, and M. Egerstedt, "Multi-oObjective Compositions for Collision-Free Connectivity Maintenance in Teams of Mobile Robots," in *2016 IEEE 55th Conference on Decision and Control (CDC)*. IEEE, 2016, pp. 2659–2664.

[12] P. Glotfelter, J. Cortés, and M. Egerstedt, "Nonsmooth Barrier Functions with Applications to Multi-Robot Systems," *IEEE Control Systems Letters*, vol. 1, no. 2, pp. 310–315, 2017.

[13] G. Vásárhelyi, C. Virágh, G. Somorjai, T. Nepusz, A. E. Eiben, and T. Vicsek, "Optimized Flocking of Autonomous Drones in Confined Environments," *Science Robotics*, vol. 3, no. 20, 2018.

[14] T. Vicsek, A. Czirók, E. Ben-Jacob, I. Cohen, and O. Shochet, "Novel Type of Phase Transition in a System of Self-driven Particles," *Physical review letters*, vol. 75, no. 6, p. 1226, 1995.

[15] R. Olfati-Saber, "Flocking for Multi-Agent Dynamic Systems: Algorithms and Theory," *IEEE Transactions on Automatic Control*, vol. 51, no. 3, pp. 401–420, 2006.

[16] L. E. Beaver, C. Kroninger, and A. A. Malikopoulos, "An Optimal Control Approach to Flocking," in *2020 American Control Conference (ACC)*. IEEE, 2020, pp. 683–688.

[17] X. Liu, X. Xiang, Y. Chang, C. Yan, H. Zhou, and D. Tang, "Hierarchical Weighting Vicsek Model for Flocking Navigation of Drones," *Drones*, vol. 5, no. 3, p. 74, 2021.

[18] C. Toumieh and A. Lambert, "Decentralized multi-agent planning using model predictive control and time-aware safe corridors," *IEEE Robotics and Automation Letters*, vol. 7, no. 4, pp. 11 110–11 117, 2022.

[19] J. Tordesillas and J. P. How, "MADER: Trajectory Planner in Multiagent and Dynamic Environments," *IEEE Transactions on Robotics*, vol. 38, no. 1, pp. 463–476, 2021.

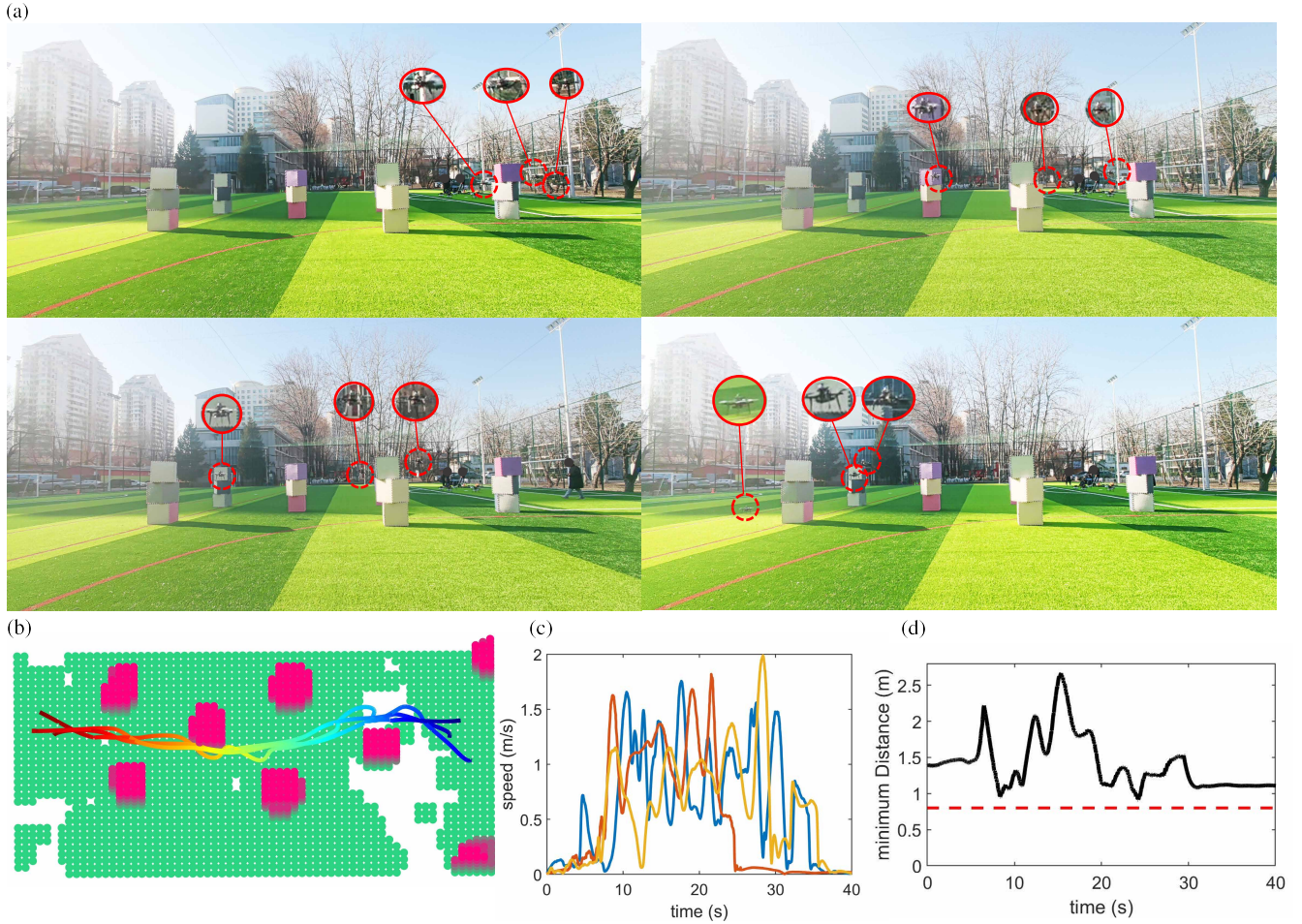[20] E. Soria, F. Schiano, and D. Floreano, "Distributed Predictive Drone

Fig. 21: The real flight experiments in scenarios 3. (a) The composite image of drone swarm flight. (b) The swarm trajectories in the point cloud maps. The trajectories at different time stamps are represented in different colors. (c) Swarm speeds and minimum distances among drones over time. The red, yellow, and blue curves represent the speed of drones 0, 1, and 2, respectively. The red dotted line represents the safety distance between drones. The black curve denotes the minimum distance among drones.

Swarms in Cluttered Environments," *IEEE Robotics and Automation Letters*, vol. 7, no. 1, pp. 73–80, 2021.

[21] C. E. Luis, M. Vukosavljev, and A. P. Schoellig, "Online Trajectory Generation with Distributed Model Predictive Control for Multi-Robot Motion Planning," *IEEE Robotics and Automation Letters*, vol. 5, no. 2, pp. 604–611, 2020.

[22] J. Park and H. J. Kim, "Online Trajectory Planning for Multiple Quadrotors in Dynamic Environments Using Relative Safe Flight Corridor," *IEEE Robotics and Automation Letters*, vol. 6, pp. 659–666, 2021.

[23] X. Zhou, J. Zhu, H. Zhou, C. Xu, and F. Gao, "EGO-Swarm: A Fully Autonomous and Decentralized Quadrotor Swarm System in Cluttered Environments," in *2021 IEEE International Conference on Robotics and Automation (ICRA)*. IEEE, 2021, pp. 4101–4107.

[24] K. Kondo, R. Figueroa, J. Rached, J. Tordesillas, P. C. Lusk, and J. P. How, "Robust MADER: Decentralized Multiagent Trajectory Planner Robust to Communication Delay in Dynamic Environments," *IEEE Robotics and Automation Letters*, 2023.

[25] Airbus. (2019) Airbus skyways: the future of the pracel delivery in smart cities. Accessed July 4, 2023. [Online]. Available: https://www.embention.com/projects/airbus-parcel-delivery/

[26] Q. Quan, R. Fu, M. Li, D. Wei, Y. Gao, and K.-Y. Cai, "Practical Distributed Control for VTOL UAVs to Pass a Virtual Tube," *IEEE Transactions on Intelligent Vehicles*, vol. 7, no. 2, pp. 342–353, 2022.

[27] Y. Gao, C. Bai, L. Zhang, and Q. Quan, "Multi-UAV Cooperative Target Encirclement within an Annular Virtual Tube," *Aerospace Science and Technology*, vol. 128, p. 107800, 2022.

[28] H. Guo, M. Chen, Y. Shen, and M. Lungu, "Distributed Event-Triggered Collision Avoidance Formation Control for QUAVs With Disturbances Based on Virtual Tubes," *IEEE Transactions on Industrial Electronics*, vol. 72, no. 2, pp. 1892–1903, 2024.

[29] Q. Quan, Y. Gao, and C. Bai, "Distributed Control for a Robotic Swarm to Pass Through a Curve Virtual Tube," *Robotics and Autonomous Systems*, vol. 162, p. 104368, 2023.

[30] Y. Rasekhipour, A. Khajepour, S.-K. Chen, and B. Litkouhi, "A Potential Field-based Model Predictive Path-planning Controller for Autonomous Road Vehicles," *IEEE Transactions on Intelligent Transportation Systems*, vol. 18, pp. 1255–1267, 2016.

[31] Y. Luo, P. Cai, A. Bera, D. Hsu, W. S. Lee, and D. Manocha, "Porca: Modeling and Planning for Autonomous Driving among Many Pedestrians," *IEEE Robotics and Automation Letters*, vol. 3, pp. 3418–3425, 2018.

[32] S. R. Nagrare, L. A. Tony, A. Ratnoo, and D. Ghose, "Multi-Lane UAV Traffic Management with Path and Intersection Planning," in *AIAA Scitech 2022 Forum*, 2022, p. 1505.

[33] P. Mao and Q. Quan, "Making Robotics Swarm Flow More Smoothly: A Regular Virtual Tube," in *IEEE/RSJ International Conference on Intelligent Robots and Systems (IROS)*, 2022, pp. 4498–4504.

[34] K. Rao, H. Yan, R. Zhang, Z. Huang, and P. Yang, "Gradient-Based Online Regular Virtual Tube Generation for UAV Swarms in Dynamic Fire Scenarios," *IEEE Transactions on Industrial Informatics*, vol. 20, no. 12, pp. 14 204–14 213, 2024.

[35] K. I. Joy, "A matrix formulation of the cubic bezier curve," *Visualization and Graphics Research Group, University of California, Davis*, 2000.

[36] R. Oberdieck, N. A. Diangelakis, I. Nascu, M. M. Papathanasiou,

M. Sun, S. Avraamidou, and E. N. Pistikopoulos, "On Multi-parametric Programming and Its Applications in Process Systems Engineering," *Chemical engineering research and design*, vol. 116, pp. 61–82, 2016.

[37] E. N. Pistikopoulos, M. C. Georgiadis, and V. Dua, *Multi-parametric Programming: Theory, Algorithms and Applications*, 2007.

[38] A. V. Fiacco, "Sensitivity Analysis for nonlinear programming using penalty methods," *Mathematical programming*, vol. 10, no. 1, pp. 287–311, 1976.

[39] F. Gao, W. Wu, W. Gao, and S. Shen, "Flying on Point Clouds: Online Trajectory Generation and Autonomous Navigation for Quadrotors in Cluttered Environments," *Journal of Field Robotics*, vol. 36, no. 4, pp. 710–733, 2019.

[40] J. Tordesillas, B. T. Lopez, M. Everett, and J. P. How, "Faster: Fast and Safe Trajectory Planner for Navigation in Unknown Environments," *IEEE Transactions on Robotics*, vol. 38, no. 2, pp. 922–938, 2021.

[41] Y. Ren, F. Zhu, W. Liu, Z. Wang, Y. Lin, F. Gao, and F. Zhang, "Bubble Planner: Planning High-Speed Smooth Quadrotor Trajectories Using Receding Corridors," in *2022 IEEE/RSJ International Conference on Intelligent Robots and Systems (IROS)*. IEEE, 2022, pp. 6332–6339.

[42] L. A. Piegl and W. Tiller, "Surface Approximation to Scanned Data," *The Visual Computer*, vol. 16, no. 7, pp. 386–395, 2000.

[43] T. Strothotte and S. Schlechtweg, "7 - Geometric Models and Their Exploitation in NPR," in *Non-Photorealistic Computer Graphics*, ser. The Morgan Kaufmann Series in Computer Graphics. Morgan Kaufmann, 2002, pp. 203–245.

[44] A. Bemporad and C. Filippi, "An algorithm for approximate multiparametric convex programming," *Computational Optimization and Applications*, vol. 35, pp. 87–108, 2006.

[45] X. Dai, C. Ke, Q. Quan, and K.-Y. Cai, "RFlySim: Automatic Test Platform for UAV Autopilot Systems with FPGA-based Hardware-in-the-loop Simulations," *Aerospace Science and Technology*, vol. 114, p. 106727, 2021.